

UC Davis

UC Davis Previously Published Works

Title

Practical limits to the use of non-intrusive load monitoring in commercial buildings

Permalink

<https://escholarship.org/uc/item/11t4v5c9>

Authors

Meier, Alan

Cautley, Dan

Publication Date

2021-11-01

DOI

10.1016/j.enbuild.2021.111308

Peer reviewed

Highly Selective and Productive Reduction of Carbon Dioxide to Multicarbon Products via in-situ CO Management using Segmented Tandem Electrodes

Tianyu Zhang¹⁺, Justin C. Bui^{2,3+}, Zhengyuan Li¹, Alexis T. Bell^{2,3}, Adam Z. Weber^{3*}, Jingjie Wu^{1*}

⁺These authors contributed equally.

¹Department of Chemical and Environmental Engineering, University of Cincinnati,
Cincinnati, OH, 45221, United States

²Department of Chemical and Biomolecular Engineering, University of California Berkeley,
Berkeley, CA, 94720, United States

³Joint Center for Artificial Photosynthesis, Lawrence Berkeley National Laboratory,
Berkeley, CA, 94720, United States

Nature Catalysis

November 18th, 2021

*Corresponding authors: azweber@lbl.gov; jingjie.wu@uc.edu

Abstract

Electrochemical CO₂ reduction provides a promising route to the sustainable generation of valuable chemicals and fuels. Tandem catalysts enable sequential CO₂-to-CO and CO-to-multicarbon (C₂₊) product conversions on distinct sites to produce high C₂₊ Faradaic efficiency (FE). Unfortunately, prior tandem catalysts exhibit poor management of CO intermediates, which diminishes C₂₊ FE. Here, we design segmented gas-diffusion electrodes (s-GDEs) in which a CO-selective catalyst layer (CL) segment at the inlet prolongs the residence time of CO in the subsequent Cu CL segment, enhancing the rate of conversion. We demonstrate that this phenomenon enables significant increases in both the CO utilization towards C₂₊ formation and C₂₊ current density for a Cu/Ag s-GDE compared to pure Cu by increasing the *CO coverage within the Cu CL. Lastly, we develop a Cu/Fe-N-C s-GDE with 90% C₂₊ FE at C₂₊ partial current density (j_{C2+}) exceeding 1 A cm⁻². These results prove the importance of transport and establishing design principles and optimization routes for heretofore unrealized j_{C2+} .

Introduction. The electrochemical reduction of CO₂ (CO₂R) to value-added chemicals provides a sustainable route to the generation of fuels and chemicals while simultaneously mitigating CO₂ emissions.^{1,2} Of the products that can be generated from CO₂R, multi-carbon (C₂₊) products are the most desirable due to their industrial value as a chemical feedstock.^{3,4} Among the catalysts explored for CO₂R, only Cu-containing materials have demonstrated the capacity to generate C₂₊ products, and many prior studies have aimed to develop catalysts exhibiting enhanced rates for C₂₊ generation. In the reaction of CO₂ to C₂₊ on Cu, the kinetics of the rate-determining step, which dictates the partial current density for C₂₊ products (j_{C2+}),⁵⁻⁹ depends on the adsorption energy of adsorbed carbon monoxide (*CO) and, subsequently, on the *CO surface coverage (θ_{*CO}).¹⁰⁻¹² Therefore, recent work has attempted to increase the binding of *CO on Cu in order to increase the rate of conversion to C₂₊.^{6,13-16} Since θ_{*CO} is determined by the concentration of CO near the catalyst, the yield of C₂₊ products on Cu can be enhanced by increasing local CO concentration.^{12,17} In particular, for vapor-fed systems that do not suffer from the concern of low CO solubility in the electrolyte, an increase in CO partial pressure has been shown to directly result in enhanced C₂₊ production.¹⁸

Cascade CO₂R systems, which integrate two consecutive steps of CO₂-to-CO and CO-to-C₂₊ on two distinct catalytic sites, can intensify the θ_{*CO} on a Cu surface.¹⁹⁻²³ In these systems, one catalyst material selectively converts CO₂ to CO to provide an *in-situ* source of CO that enhances θ_{*CO} , and another Cu-containing catalyst performs C-C coupling. The state-of-the-art bimetallic tandem catalysts, such as Cu/Ag and Cu/FeTPP[Cl], exhibit substantially reduced overpotential, enhanced Faradaic efficiency (FE) to C₂₊ (~85%), and improved C₂₊ partial current density ($j_{C2+} = \sim 300 \text{ mA cm}^{-2}$) relative to pure Cu catalysts.^{24,25} Since the θ_{*CO} is often the limiting factor, higher j_{C2+} values can be achieved by increasing the local CO partial pressure (P_{CO}) with increased CO generation rates.^{12,26,27} However, if the rate of CO generation exceeds the rate of C-C coupling, CO utilization and C₂₊ FE are diminished.^{20,22,25,28} This tradeoff presents a need to manage *in situ* CO formation in order to maximize the C₂₊ FE while still maintaining high j_{C2+} .^{29,30}

Our prior studies have demonstrated the value of a layered gas-diffusion electrode (l-GDE) structure (see **Figure 1c**), in which a CO-selective catalyst layer (CL) is placed on top of a C₂₊-selective Cu CL.^{29,30} The l-GDE was inspired by the higher reactant conversion in a plug-flow reactor (PFR) compared to that in a continuous-stirred-tank reactor (CSTR) for reactions with a positive reaction order.³¹ In a PFR, this enhancement in conversion results from increased residence time within the reactor. By creating a layered CL structure in the through-plane direction of the GDE (z -axis in **Figure 1a**), it is possible to concentrate the CO at the Cu CL/electrolyte interface and dimerize CO progressively along the z -axis, imitating the reactant concentration profile in a PFR. This layered structure intensifies the local θ_{*CO} within the Cu CL and boosts j_{C2+} by a factor of 1.2 compared to that for a pure Cu GDE.³⁰ Unfortunately, the l-GDE only controls the P_{CO} profile along the z -axis at the micrometer scale and fails to manage

P_{CO} profile along the electrode length (y -axis in **Figure 1a**) at the centimeter scale. Consequently, there is a significant opportunity for further enhancement of θ_{*CO} and j_{C_2+} .

Here, we present a segmented gas-diffusion electrode (s-GDE) structure for selective CO_2R to C_{2+} . The s-GDE integrates a CO-selective CL segment at the inlet end of the GDE and a Cu CL segment down the rest of the GDE, enabling spatial management of θ_{*CO} in-plane along the length of the electrode (y -direction). Two structures of s-GDEs (stacked and co-planar) comprising Ag and Cu CL segments are displayed in **Figure 1a-b**. In the stacked configuration, the Cu and Ag CL segments are present in distinct layers in both the y - and z -directions. In the co-planar configuration, the Cu and Ag CL segments are in a single layer in the z -direction but are still distinct in the y -direction. In both cases, the Ag CL segment aligns with the CO_2 gas inlet to enable rapid conversion of the incoming CO_2 into a supplementary CO supply that enhances the θ_{*CO} and can be converted to C_{2+} products over the subsequent Cu CL segment (analogous to reactant conversion in a PFR). Guided by theoretical studies of mass transport, we optimize the CO residence time. Using the insights gained and to prove their universality, we develop an s-GDE consisting of Cu and single-atom iron (Fe-N-C) CL segments capable of achieving unprecedented C_{2+} FE and j_{C_2+} .

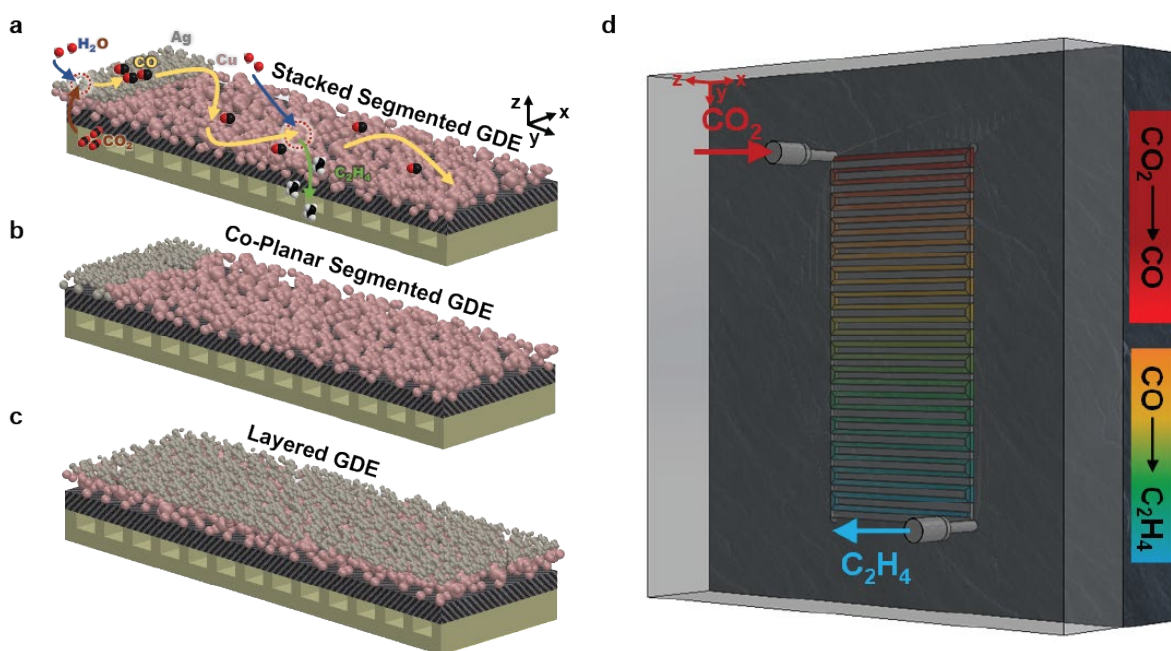


Figure 1. Concept of segmented tandem gas-diffusion electrodes. Schematic of (a) stacked and (b) co-planar segmented gas-diffusion electrodes. For comparison, the structure of the layered gas-diffusion electrode is also displayed in the bottom panel (c). The arrows in (a) represent the reaction and mass transport of the proposed tandem reaction process in the catalyst layer. (d) Schematic of the flow-channel geometry and gas concentration changing along the flow channel during the tandem reaction of $\text{CO}_2 \rightarrow \text{CO} \rightarrow \text{C}_2\text{H}_4$.

Along-the-channel conversion of generated CO in a s-GDE. To understand the relationship between the P_{CO} and the rate of CO conversion, we performed a series of experiments that

enabled tracking of the local P_{CO} and the $j_{\text{C2+}}$ within individual segments along the length (y -direction) of the s-GDE. Using the stacked s-GDE as a model geometry, the change of the local P_{CO} and C_{2+} productivity along the y -axis was mapped indirectly by measuring the CO outflow rate and the $j_{\text{C2+}}$ from six modified s-GDEs (See **Methods** for details). The resulting modified s-GDEs (E1 to E6) are 0.50 cm wide and possess a condensed 0.2 cm long Ag CL stacked on top of a Cu CL that varies from 0.2 (E1) to 2.0 cm (E6) (**Figure 2a**). CO_2R performance of these six electrodes (E1 to E6) was evaluated in a membrane-electrode-assembly (MEA) electrolyzer (See **Methods** for details).

By plotting the FE enhancements observed by extending the length of the Cu CL (**Figure 2c** and **Supplementary Figure S1**), it is observed that as the Cu CL segment is extended from E1 to E6, the FE to CO gradually declines from 65.5 to 6.2%, while the overall FE of C_{2+} products rises from 33.2 to 82.0%. The FE to a specific C_{2+} product (C_2H_4 , $\text{C}_2\text{H}_5\text{OH}$, CH_3COO^- , and $\text{C}_3\text{H}_7\text{OH}$) exhibits similar behavior as the overall C_{2+} FE (**Supplementary Figure S4**). This trend indicates that as the Cu CL is extended, the residence time of CO (generated within the Ag CL) increases within the Cu CL thereby enabling better conversion to C_{2+} products. However, the FE gradient ($|\Delta\text{FE}/\Delta L|$) of both CO and C_{2+} products declines as the Cu CL length increases, indicating that there is a length beyond which no further FE enhancements are observed because all the *in-situ* generated CO has been consumed. This theory is further corroborated by plotting the CO utilization, defined as the percentage of CO generated within the s-GDE that is converted to C_{2+} products (see **Supplementary Note S1**) as a function of the Cu CL length. As shown in **Figure 2d**, as the Cu CL length increases, the CO utilization towards C_{2+} formation increases, achieving a maximum value of 0.82.

To understand the enhancements in conversion, it is critical to understand the profile of the P_{CO} and C_{2+} mass activity (defined as the partial current for C_{2+} products normalized by the mass loading of Cu in the catalyst layer) within the modified s-GDE. The C_{2+} mass activity decreases as the Cu CL length increases and more CO is converted to C_{2+} products (**Figure 2d**). Therefore, the conversion of *in-situ* generated CO to C_{2+} leads to a decay in P_{CO} down the length of the s-GDE (depicted in **Figure 2b**). The corresponding decrease in mass activity to C_{2+} products as the electrode length increases also suggests that $j_{\text{C2+}}$ is largely dependent on the local concentration of CO, rather than the local concentration of fed CO_2 , which due to the high stoichiometry of the feed gas (~ 10 times the amount of CO_2 required to achieve stoichiometric conversion at 1 A cm^{-2} of CO_2R), will be relatively constant throughout the s-GDE.^{32,33} It is important to note that the electrochemically active surface area (ECSA) increases linearly with the Cu CL length (**Supplementary Figure S5**). Therefore, the increase in ECSA alone upon extending the Cu CL is insufficient to explain the nonlinear trends observed for the CO and C_{2+} partial current densities (**Supplementary Figure S4**), providing further evidence that the enhanced residence time of *in-situ* generated CO in the extended Cu CL enables improved $\theta_{*\text{CO}}$ and thus $j_{\text{C2+}}$. It is noteworthy that while there is likely a large amount of CO generated

in the Cu CL (Supplementary Figure S6 and Supplementary Note S2), it appears that the trends in j_{C_2+} are largely driven by the residence time of the *in-situ* generated CO. Placing the CO-selective catalyst at the inlet of the s-GDE leverages the along-the-channel transport within the MEA to distribute and subsequently further reduce the entrance CO from the Ag. However, for the layered GDE, the *in-situ* generated CO can easier exit the Cu CL prior to conversion.

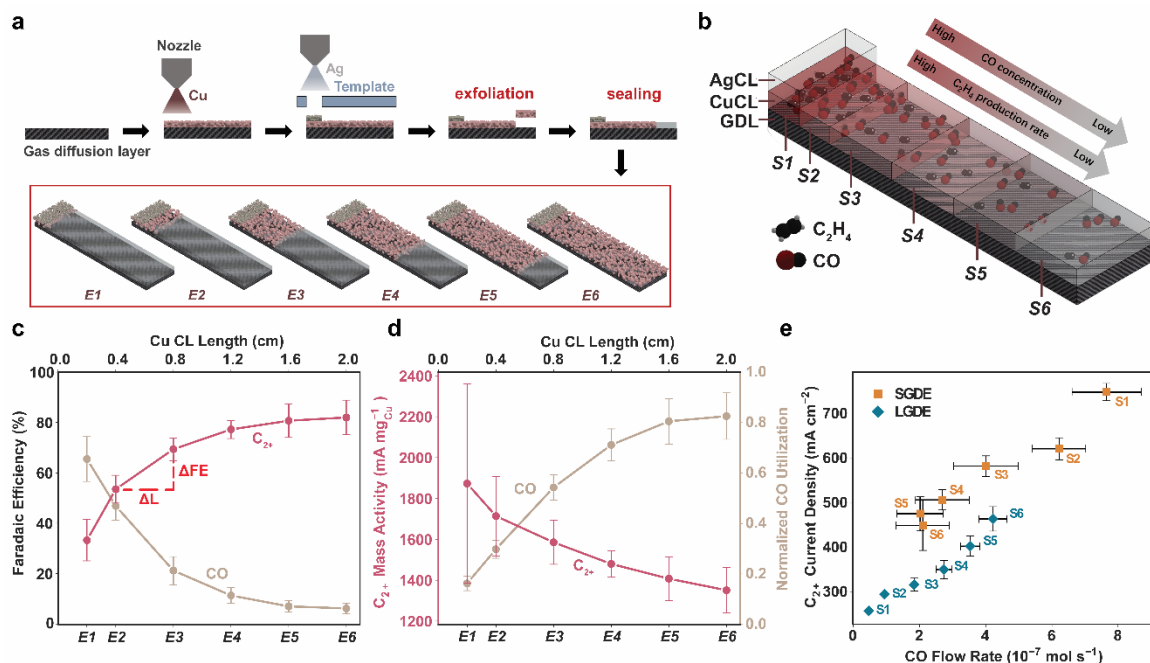


Figure 2. Along-the-channel conversion of generated CO in a s-GDE. (a) Schematic of the s-GDE preparation procedure. The geometries of six s-GDEs (from E1 to E6) with a constant dimension of the Ag CL (L: 0.20 cm, W: 0.50 cm) and a varied dimension of the Cu CL (L: 0.20 ~ 2.00 cm, W: 0.50 cm) are shown in the inset. (b) Schematic of decreasing C_{2+} mass activity, along with the decreasing CO concentration along the y-axis of s-GDE. (c) FE to CO (light brown) and C_{2+} products (dark red) versus the Cu CL length at a cathodic potential of -0.70 V vs. RHE, calculated by subtracting the anode potential from the IR-corrected applied cell voltage (Supplementary Figures S2-3). (d) CO utilization towards C_{2+} formation (light brown curve) and C_{2+} mass activity (dark red curve) versus the Cu CL length. (e) Local j_{C_2+} plotted against local CO outflow rate in the six sub-segments (S1 to S6) of the s-GDE and l-GDE. The sub-segment S_i represents the difference of two Cu CL segments in two consecutive electrodes (for example, $S1 = E1$; $S_i = E_i - E_{i-1}$, $6 \geq i \geq 2$) and is labeled in (b). The error bars represent the standard deviation from the measurement of three independent electrodes. C_{2+} current measured is primarily toward the generation of C_2H_4 and C_2H_5OH (Supplemental Figure S4).

To elucidate further the interplay between the local P_{CO} and the rate of C_{2+} generation in the s-GDE, the local CO flow rate is plotted versus j_{C_2+} for each sub-segment, as shown in Figure 2e (see Methods for details). The sub-segment S_i is defined as the difference of the Cu CL segments between two consecutive electrodes, and all sub-segments are labeled schematically in Figure 2b. The gas feedstock flows from S1 to S6. The local CO flow rate in Figure 2e represents the outlet flow rate for the full electrode E_i , which is indicative of the local CO flow rate and the P_{CO} in each sub-segment S_i . Because these flow rates represent the outlet flow

rates exiting from the last segment in each electrode, the CO flow rates measured here comprised only the CO generated in the s-GDE that is not consumed to form C_{2+} products. Most of the generated CO in these tandem electrodes is consumed to form C_{2+} products, explaining the low calculated outlet CO flow rates.

The local CO flow rate gradually decreases by 73% from S1 to S6 in the s-GDE due to the CO consumption. As expected, this decline is accompanied by the decrease of $j_{C_{2+}}$ from 749.2 (S1) to 450.0 mA cm^{-2} (S6). Nonetheless, while the $j_{C_{2+}}$ decreases from S1 to S6, the FE to C_{2+} products increases from S1 to S6. This apparent contradiction can be explained as follows. Because of the large source of supplemental CO from the Ag catalyst, S1 possesses the highest local CO concentration and thus the largest C_{2+} current density. However, as discussed previously, most of the CO in S1 is not properly utilized. Therefore, even though this segment generates a substantial amount of CO, a substantial amount of that CO exits the segment before it is converted to C_{2+} products, explaining the low C_{2+} FE and high CO FE.

When performing the same analysis of the relationship between local CO flow rate and C_{2+} productivity in sub-segments of l-GDEs (see **Methods** for details), similar behavior is observed. These modified l-GDE electrodes (E1 to E6) possess stacked Ag and Cu CLs of equal length that vary from 0.20 cm (E1) to 2.00 cm (E6) (**Supplementary Figures S7-9**) with the Ag and Cu mass of E6 for the l-GDE and s-GDE being equivalent. As the CO flow rate in the l-GDE increases, the $j_{C_{2+}}$ increases at a rate identical to that of the s-GDE, with both the plots of the s-GDE and l-GDE CO flow rates vs. C_{2+} current densities possessing linear slopes of $5 \times 10^9 \text{ C m}^{-2} \text{ mol}^{-1}$. The fact that the trend of the sub-segment $j_{C_{2+}}$ exhibits a linear relationship with the local CO flow rate supports our hypothesis that the C_{2+} production rate depends primarily on P_{CO} . However, it is important to note that at an equivalent CO flow rate, the l-GDE possesses lower C_{2+} current density than the s-GDE, which is due to differences in the *in-situ* CO management along the y-axis. Due to the more PFR-like nature of the s-GDE, the residence time, and thus the rate of conversion, is higher for the s-GDE than for the l-GDE, even for equivalent CO flow rates. The enhanced concentration of CO and θ_{*CO} in the s-GDE structure promotes greater $j_{C_{2+}}$.

Effect of Cu:Ag area ratio on the performance of s-GDEs for CO₂ reduction. To further assess the impact of the spatial management of CO concentration on the rate of C_{2+} production within s-GDEs, five different stacked Cu/Ag s-GDEs with varying ratios of Cu and Ag CL areas were prepared and tested. The area of the Cu CL was held at 1.00 cm^2 , while the Ag CL had the same width, but its length was varied from 0.10 cm to 2.00 cm (*i.e.* its area varied from 0.05 to 1.00 cm^2) (**Figure 3a-b**). These s-GDEs are denoted as Cu/Ag (x:y) s-GDE, where x and y represent the area of the Cu and Ag CLs, respectively. A pure Cu GDE was also prepared for comparison. The mass of Cu was maintained at 0.40 mg while the corresponding Ag mass was optimized to maximize CO utilization rates and kept the same for all s-GDEs (**Supplementary Figure 10**). Because the Ag mass is kept constant for all Ag CL areas, the

thickness of the Ag CL segment grows as its area shrinks. **Figure 3c and d** show the cross-sectional SEM and EDS of the two CLs overlapping section in the Cu/Ag (1.00:0.05) s-GDE, which has the thickest Ag CL in this study. The total thickness of the CL in the overlapping area is $\sim 2.0 \mu\text{m}$, including $0.5 \mu\text{m}$ for the Ag CL, which is still thin enough so as to not produce mass-transport limitations, in accordance with our previous work.^{29,30}

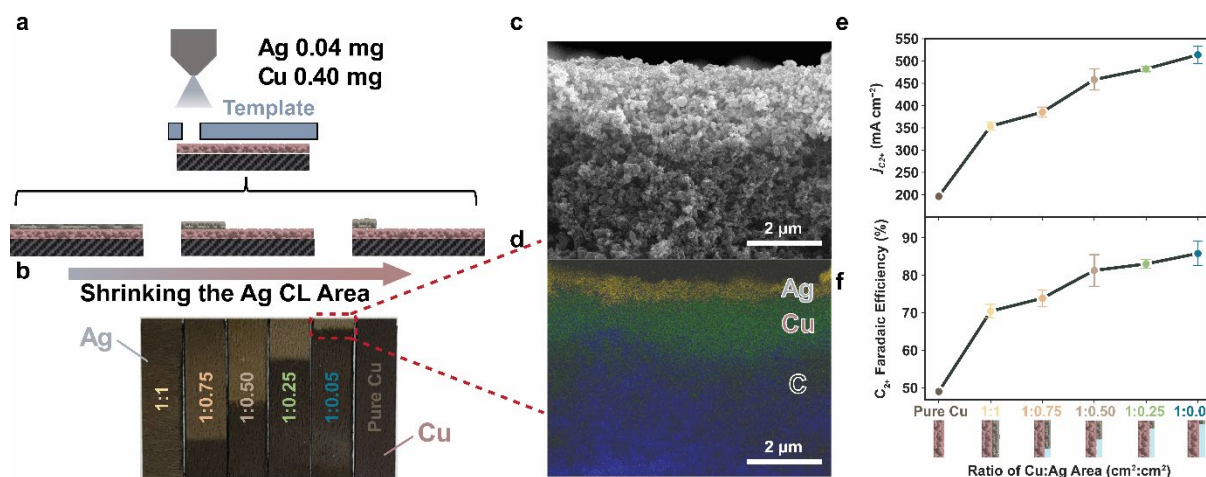


Figure 3. Effect of Cu:Ag area ratio on the performance of s-GDEs for CO₂ reduction. (a) The schematic of the preparation procedure of five s-GDEs with fixed quantities of Cu and Ag catalysts but a varied area ratio between Cu and Ag CLs. **(b)** Photos of five Cu/Ag (x:y) s-GDEs and a control Cu GDE. *x* and *y* represent the area of the Cu and Ag CLs, respectively. **(c)** The cross-sectional SEM image and **(d)** EDS elemental mapping of the overlapping section in the Cu/Ag (1.00:0.05) s-GDE. **(e)** The C₂₊ Faradaic efficiency and **(f)** $j_{\text{C}_{2+}}$ as a function of the ratio of the Cu:Ag CL areas at a constant applied cell voltage of 3.05 V. The error bars represent the standard deviation from the measurement of three independent electrodes.

As shown in **Figure 3e-f**, all s-GDEs offer an improved yield of C₂₊ products compared to the Cu GDE at an equivalent applied cell voltage. The product distributions, total current densities, and partial current density of C₂₊ products for all tested GDEs are shown in **Supplementary Figures S11 and S12**. For the s-GDEs, both the FE of C₂₊ products (**Figure 3f**) and $j_{\text{C}_{2+}}$ (**Figure 3e**) rise gradually as the Ag CL area shrinks from 1.00 cm² to 0.05 cm². The Cu/Ag (1.00:0.05) s-GDE exhibits the highest C₂₊ FE and $j_{\text{C}_{2+}}$ because it produces the highest concentration of CO and in accordance with the results shown in **Figure 2**, achieves the highest CO utilization. The Cu/Ag (1.00:0.05) s-GDE achieves a maximum FE of C₂₊ of 86.1% and $j_{\text{C}_{2+}}$ of 559.5 mA cm⁻² at a cell voltage of 3.16 V. The cell voltage reported here is IR compensated unless otherwise stated. The internal cell resistance varies with different contact resistances and membrane ionic resistance. IR compensation enables a more rigorous comparison of the kinetic performance between different tandem electrodes by deconvoluting the variable effects of cell assembly and membrane conductivity. Moreover, the electrochemical testing used a strong alkaline electrolyte (0.5 M KOH) to reduce the applied overpotential. Therefore, the cell voltages reported here are only for comparison with devices operated in similar conditions with IR-

correction. Nonetheless, these values correspond to a $1.7\times$ increase in C_{2+} FE and a $2.7\times$ increase in $j_{C_{2+}}$ compared to a pure Cu GDE at the same applied cell voltage. **Supplementary Figure S13** shows that the yields of C_2H_4 and C_2H_5OH as a function of Ag CL area follow similar trends. Notably, all s-GDEs exhibit lower FE and partial current density of CO than the Cu GDE (**Supplementary Figure S14**), which translates to a greater CO utilization. Furthermore, the residence time of the *in-situ* generated CO was estimated for each s-GDE (**Supplementary Note S3**), demonstrating that the average residence time of the CO increases as the ratio of Cu/Ag area is increased. This increase in the CO utilization and residence time for the s-GDE when compared to the Cu GDE implies that the increased θ_{*CO} not only allows for greater conversion of the *in-situ* generated CO, but also enables increased conversion of the Cu-generated $*CO$ intermediates by mass action.

The value of θ_{*CO} along the y -axis is controlled by two critical factors, the area ratio and spatial arrangement of the Cu and Ag CL segments. The Ag layer must be placed at the inlet to exploit the along-the-channel gradients and enhance θ_{*CO} . However, the out-of-plane overlap between Cu and Ag CLs segments in the stacked s-GDE configuration is not necessarily required. Apart from the stacked Cu/Ag (1.00:0.05) s-GDE, an alternative s-GDE was prepared, which has co-planar Cu and Ag CL segments (**Figure 1b**) with areas of 0.95 and 0.05 cm^2 , respectively. The co-planar Cu/Ag (0.95:0.05) s-GDE exhibits comparable activity and C_{2+} FE as the stacked Cu/Ag (1.00:0.05) s-GDE (**Supplementary Figure S15**). This result demonstrates that along-the-channel gradients in the y -direction dominate with regard to enhancing residence time and $j_{C_{2+}}$ rather than through-plane transport in the z -direction.

Multiphysics model of mass transport and CO adsorption in an s-GDE. A 2D continuum model of the cathodic chamber of the cell was developed to rationalize and guide the results and design, respectively. Multiple prior studies in aqueous electrolytes have shown that the generation of C_{2+} products from CO follows an approximately first-order rate dependence on CO concentration at low CO partial pressures, for which the fraction of empty Cu sites is near unity.^{2,9,26,34-38} This rate order is consistent with the linear trends observed in **Figure 2e** and is consistent with prior experimental studies of CO reduction (COR).^{9,12,26,30,34} However, recent studies of vapor-phase COR have demonstrated that appreciable θ_{*CO} can be achieved in porous catalyst layers, causing the rate order with respect to CO concentration to decrease as the partial pressure increases, a behavior captured by a Langmuir adsorption model (**Supplementary Figure S16**).^{12,30} This Langmuir adsorption model was implemented in a multiphysics simulation of gas-phase CO and CO_2 transport within the s-GDE and flow channel (shown schematically in **Figure 4a**) to estimate the local θ_{*CO} in experimentally tested s-GDEs (see the **Supplementary Methods** section for a more detailed discussion). It is important to note that the simulation assumes the s-GDE behaves as a perfect tandem. In other words, all C_{2+} products are derived from CO generated over Ag, as opposed to the direct reduction of CO_2 on Cu. While indeed a simplification, this assumption is relatively consistent with the results

shown in **Figure 2**, which suggest that the trends in j_{C2+} are largely driven by the consumption of *in-situ* generated CO. Additionally, the results in **Supplementary Figure S12** demonstrate that at any given voltage, j_{C2+} is significantly lower for the case of pure Cu GDE, thus implying that the rate of CO₂ conversion is much slower than that of CO.

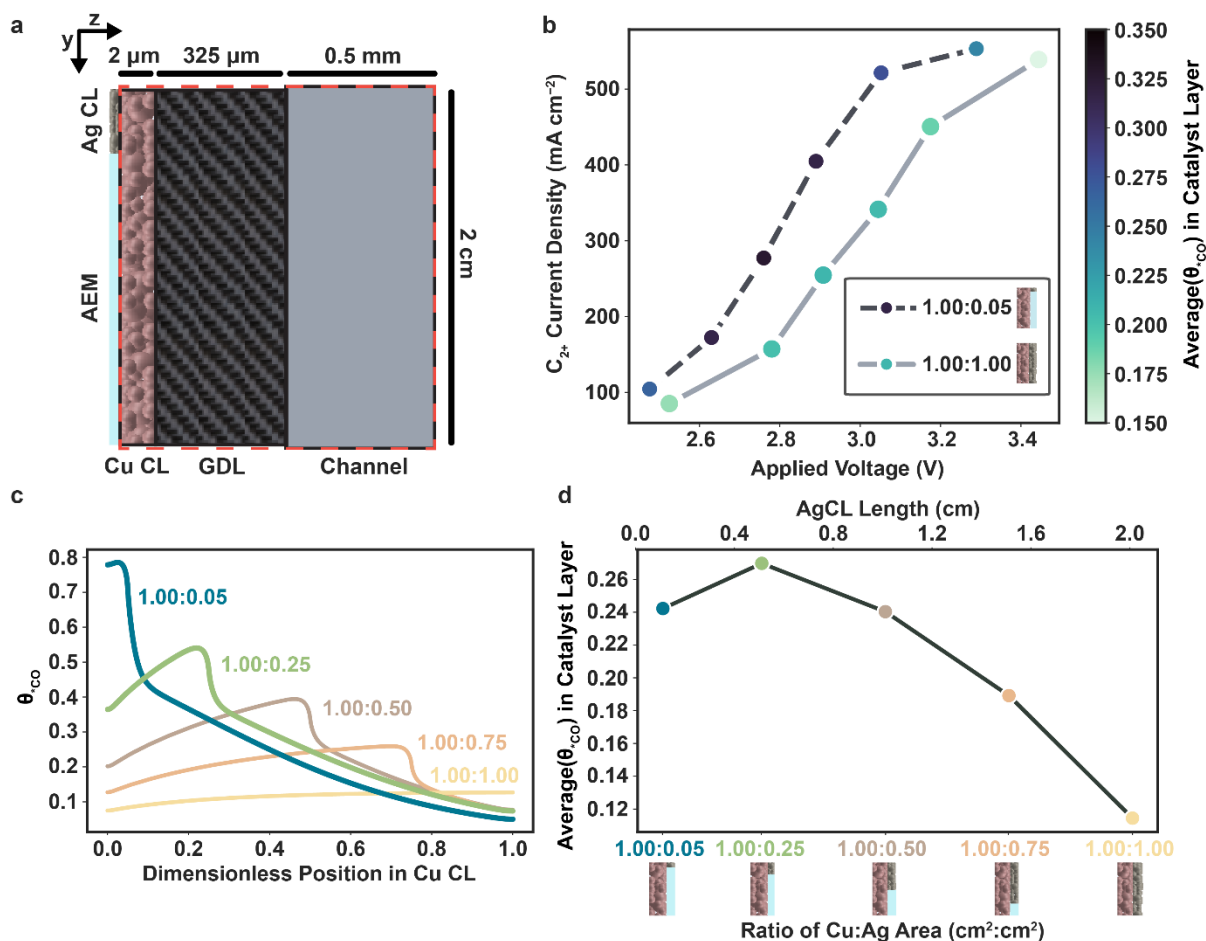


Figure 4. Multiphysics model of mass transport and CO adsorption in an s-GDE. (a) Schematic of the modeled domain (red dotted box). **(b)** Polarization curves for the Cu/Ag (1.00 : 0.05) s-GDE and (1.00 : 1.00) s-GDE. Color of the marker represents the average θ_{*CO} surface coverage attained in the Cu CL for a given Cu/Ag area ratio, voltage, and C_{2+} current density. **(c)** Simulated profiles of local θ_{*CO} in the Cu CL for all five Cu/Ag area ratios studied experimentally at a C_{2+} current density of $550\ mA\ cm^{-2}$. **(d)** Average local θ_{*CO} in the Cu CL versus Cu/Ag area ratio at a C_{2+} current density of $550\ mA\ cm^{-2}$.

As shown in **Figure 4b** and **Supplementary Figure S17**, moving from an l-GDE (Cu/Ag 1.00:1.00) to an s-GDE with a highly concentrated Ag layer (Cu/Ag 1.00:0.05) significantly increases the average value of θ_{*CO} achieved within the catalyst layer. This phenomenon can be explained as follows. As the Cu:Ag area ratio increases, the formation of CO in the Ag CL occurs in a concentrated end, thereby raising the local concentration of CO, resulting in an increased θ_{*CO} locally near the Ag/Cu boundary that decays along the length of the Cu CL as CO is consumed to form C_{2+} . This change in θ_{*CO} profile with increasing Cu/Ag area ratio is

reflected in the simulations shown in **Figure 4c** and is consistent with above results. **Figure 4d** shows the average θ_{*CO} achieved in the CL as a function of the Cu/Ag area ratio at constant j_{C2+} , demonstrating that for the same j_{C2+} , the average θ_{*CO} in the Cu CL increases as the length of the Ag layer shrinks. This increase in the average θ_{*CO} enhances j_{C2+} by mass action and corresponds to a decrease in the required overpotential to achieve the identical C_{2+} current density, consistent with the shift in overpotential observed experimentally in **Supplementary Figure S12**. The simulations provide significant evidence for the hypothesis that a higher average θ_{*CO} is achieved in s-GDEs.

It is important to note, however, that the simulations do not predict an increase in the average value of θ_{*CO} going from a Cu/Ag area ratio of 1.00:0.25 to 1.00:0.05, despite the enhancement in the j_{C2+} observed experimentally. This discrepancy can be rationalized as follows: First, the simulation is 2D, and does not account for in-plane transport along the width of the electrode (x -direction), because these gradients are likely small due to the uniformity of the s-GDE in the x -direction. However, to capture fully the enhancements going from Cu/Ag 1.00:0.25 to 1.00:0.05, it may be necessary to develop a full 3D model that accounts for the serpentine flow channel. Secondly, when considering the average P_{CO} in the Cu CL as a function of the area ratio (**Supplementary Figure S18**), an increase is observed from 1.00:0.25 to 1.00:0.05. The fact that the average P_{CO} continues to increase while the average θ_{*CO} does not is because the rate order with respect to P_{CO} is decreasing with increased partial pressure, and over-concentrating CO hampers CO re-distribution and θ_{*CO} as simulated. This turning point is not observed experimentally, suggesting that the fit Langmuir behavior may not be fully accurate. Nonetheless, the simulation generally agrees with and explains the experimental results.

The simulations presented here underscore the importance of optimizing the flow rate of the CO_2 feed gas in tandem catalysis. As shown in **Supplementary Figure S19**, for a Cu/Ag (1.00:0.05) s-GDE there is an optimal CO_2 flow rate of ~ 20 sccm for which a maximum average θ_{*CO} can be achieved. This optimum feed flow rate matches that chosen for experiment and can be justified by analysis of the simulated transport of CO generated in the Ag CL of an s-GDE. The CO generated over Ag transports out of the CL and back into the flow-channel. In the flow channel, the CO_2 acts as a carrier gas to provide convection of CO down the channel where it is re-distributed along the length of the Cu CL (**Supplementary Figure S20**). Therefore, if the molar flow rate of the CO_2 feed is too low, there is insufficient convective flux to carry the generated CO down the length of the channel where it can be adsorbed and react on the Cu CL segment. However, for an excessively high feed rate, the CO will be preferentially swept out of the flow channel, as opposed to being re-distributed into the Cu CL. The existence of an optimum molar flow rate of CO_2 has been demonstrated in prior studies of CO_2R on Cu,^{21,39,40} and further demonstrates the importance of optimizing mass transport.

The compatibility between Cu and CO-selective catalysts. CO-selective catalysts, such as

Ag, ZnO, and emerging single-atom catalysts (*e.g.*, iron-nitrogen-carbon (Fe-N-C) nanostructure), exhibit dramatically different performance for CO evolution at a given applied voltage (**Supplementary Figure S21**). The effectiveness of the s-GDE requires compatible overpotentials to produce CO in the CO-selective CL and subsequently dimerize that CO in the Cu CL. To determine the optimal catalyst pairing, we compared s-GDE performance for three CO-selective catalysts: Ag, ZnO, and Fe-N-C. For fair comparison, the catalyst loading, electrode structure, and spatial orientation of the Cu/ZnO and Cu/Fe-N-C s-GDEs were equivalent to those of the optimized Cu/Ag (1.00:0.05) stacked s-GDE (**Figure 1a**). Fe-N-C requires the lowest overpotential for maximum C_{2+} production, followed by Ag and ZnO (**Figure 5a**, **Supplementary Figures S22-S24**. **Supplementary Figure S22** demonstrates the full cell voltage without IR correction). Therefore, the Cu/Fe-N-C s-GDE presents the greatest opportunity to generate C_{2+} products at low overpotential, achieving a maximum C_{2+} FE of 87.3% and $j_{C_{2+}}$ of 437.2 mA cm^{-2} at 2.89 V (**Figure 5a** and **Supplementary Figure S23**). The C_2H_4 FE accounts for 46.9% at this cell voltage (**Supplementary Figure S24**).

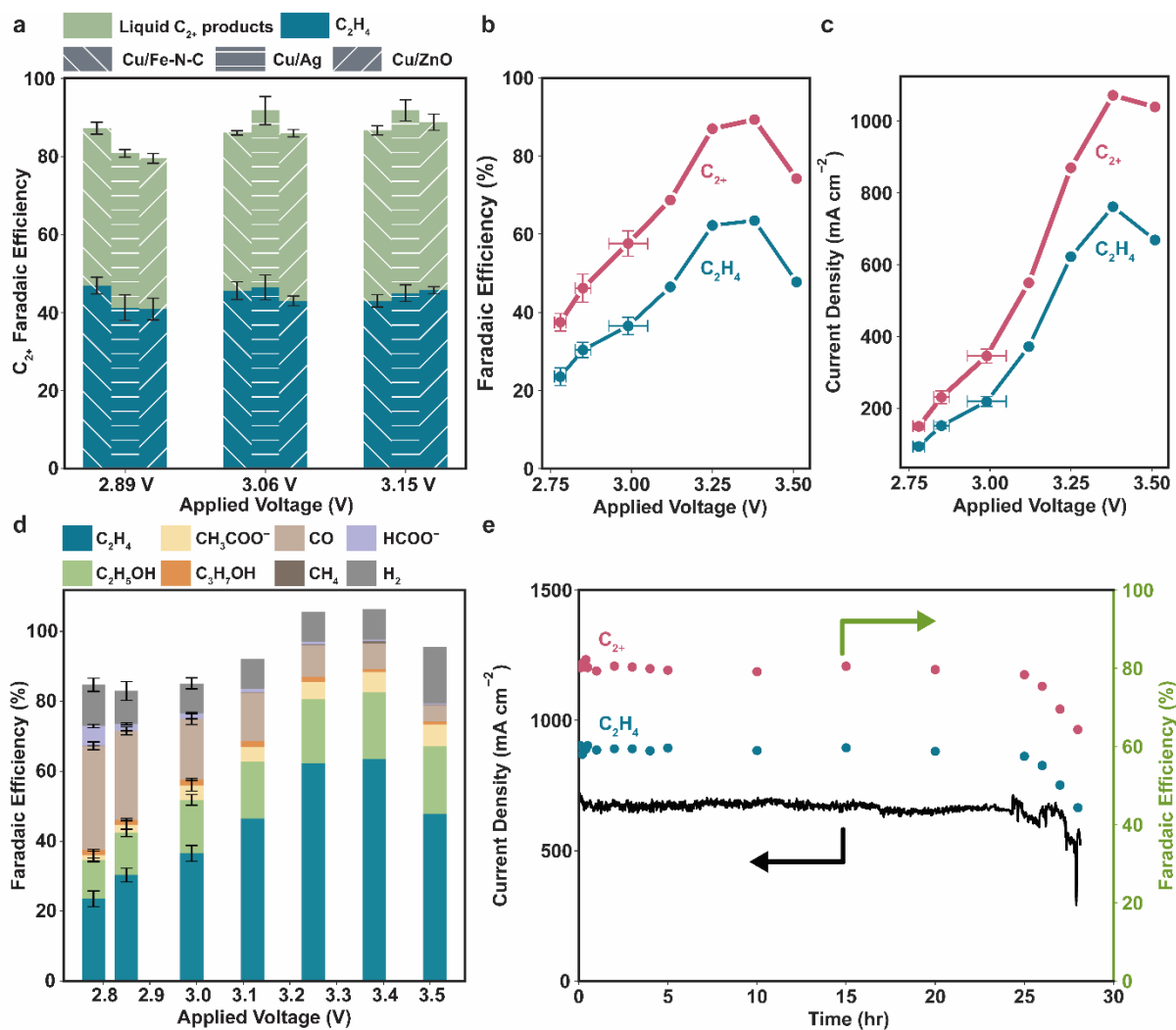


Figure 5. The compatibility between Cu and CO-selective catalysts. (a) The Faradaic efficiency of C_2H_4 and C_{2+} liquid products for Cu/Fe-N-C, Cu/Ag, and Cu/ZnO s-GDEs at

three cell voltages as operated in a MEA cell. The Cu/Fe-N-C, Cu/Ag, and Cu/ZnO s-GDEs achieve their optimal C₂H₄ FE at 2.89, 3.06, and 3.15 V, respectively. **(b)** FE and **(c)** partial current densities of C₂H₄ and C₂₊ products as a function of cell voltage on doubly-loaded Cu/Fe-N-C s-GDE as conducted in a flow cell with a thin 0.5 M KOH layer of 2 mm. **(d)** Full product distribution of doubly-loaded Cu/Fe-N-C s-GDE. **(e)** Long-term stability of Cu/Fe-N-C s-GDE operated in a thin buffer flow cell at 3.40 V. The error bars represent the standard deviation from measurements of at least three independent electrodes.

Seeking to achieve higher $j_{C_{2+}}$ on the Cu/Fe-N-C s-GDE, both the Cu and Fe-N-C loadings were doubled (i.e., Cu loading of 0.80 mg cm⁻²). Since severe flooding resulting from enhanced electroosmotic transport restricted the operation of the MEA electrolyzer to current densities under 1,000 mA cm⁻², experiments with the doubly-loaded Cu/Fe-N-C s-GDE were transferred to a flow cell equipped with a thin buffer layer (2 mm) in the cathodic compartment, between the membrane and the catalyst layer.^{41,42} The electrolyte stream reduces the water chemical potential gradient and enables high current operation at the cost of the increased cell resistance (0.20 ~ 0.60 Ω for the MEA cell versus 1.00 ~ 1.10 Ω for the flow cell) (**Supplementary Figure S2**). After doubling the loading, the Cu/Fe-N-C s-GDE achieves an $j_{C_{2+}}$ of 1071.7 mA cm⁻² and a C₂₊ FE of 89.3% at 3.38 V (**Figure 5b-d** and **Supplementary Figure S25**). These values correspond to 1.8× and 1.2× increases in the $j_{C_{2+}}$ and C₂₊ FE, respectively, compared to those for a pure Cu GDE tested in the flow cell under identical conditions (**Supplementary Figure S26**). Moreover, the C₂H₄ FE rises to 63.5% at an $j_{C_{2H_4}}$ of 761.7 mA cm⁻². The half-cell energy efficiency to C₂H₄ in the flow cell is 40.1%, while the full-cell energy efficiency is 16.9% due to high ohmic resistance in the cell with the thin electrolyte layer (**Supplementary Figure S27**, see **Methods** for description of efficiency calculation).

Long-term stability and CO₂ crossover. The flooding of the CL restricts the long-term operation at current densities exceeding 500 mA cm⁻² in the MEA electrolyzer (**Supplementary Figure S28**). Therefore, the long-term durability of Cu/Fe-N-C s-GDE was assessed in the flow cell. The Cu/Fe-N-C s-GDE maintained over 80 and 60% FEs to C₂₊ products and C₂H₄, respectively, for 24 h at an operating j_{total} of 680 mA cm⁻² (**Figure 5e**). After 24 h, the j_{total} fluctuated, and the FEs to C₂₊ products and C₂H₄ decayed due to pressure build-up in the CO₂ feed, accompanied by electrolyte flowing out from the gas flow channel and, subsequently, a short supply of CO₂ reactants. Decreasing the j_{total} to 430 mA cm⁻² prolonged durability to almost 120 h; however, the FEs to C₂H₄ (45%) and C₂₊ products (70%) were lowered (**Supplementary Figure S29**).

Another significant challenge in the development of MEAs for CO₂R is mitigating the crossover of the feed CO₂ through the anion-exchange membrane in the form (bi)carbonate anions. When calculating the carbonate crossover of the Cu/Fe-N-C s-GDE (see **Methods**), it is observed that such crossover consumes 22.5% of the total CO₂ feedstock. Previous work has demonstrated that the carbon crossover can be lessened with an acidic or neutral catholyte,^{43,44} or by employing a bipolar membrane (BPM).⁴⁵ The use of acidic electrolytes or BPMs is

beyond and ancillary to the scope of the present work; the presented results and understandings should equally apply to any CO₂ crossover mitigation strategy. However, to mitigate the crossover and to provide another point of comparison between our study and literature, CO₂ reduction with the Cu/Fe-N-C s-GDE was also performed in a MEA cell using 0.1 M KHCO₃ anolyte (**Supplementary Figure S30**). As expected, the carbonate crossover declines from 22.5% to 17.5% of the total, which, while not a substantial suppression of the crossover, is a marked improvement. However, the achievable current density also declines compared to that observed for 0.5 M KOH due to increased ohmic resistance through the membrane and higher kinetic overpotentials for CO₂R at the cathode and OER at the anode.⁴⁶ Nevertheless, the performance remains quite competitive with prior studies in 0.1 M KHCO₃ electrolyte (**Supplementary Table S4**), showing the generality of the findings. Future work should seek to employ these engineered tandem electrodes in cells with crossover mitigation strategies (*e.g.*, BPMs, acidic electrolytes) to further enhance single-pass conversion of the fed CO₂.

Conclusions. Tandem catalysts designed to convert CO₂ into C₂₊ products must efficiently manage the CO intermediate to achieve high FE for C₂₊ at high j_{C2+} . In this work, we designed a simple yet efficient s-GDE in which a short, heavily loaded CO-selective CL segment placed at the inlet of the s-GDE prolongs the residence time of generated CO in the subsequent Cu CL segment where C-C coupling takes place. By optimizing the relative lengths and loadings of Cu and Ag in a Cu/Ag s-GDE, we maximized the residence time of CO in the Cu CL segment to facilitate a 300% increase in CO utilization compared to a non-segmented Cu/Ag GDE. Moreover, we found that a 250% increase in j_{C2+} relative to pure Cu could be achieved using an optimized Cu:Ag area ratio of 1.00:0.05. A 2D-continuum model verified the effects of CL area ratios, residence time, and feed flow rate on the θ_{CO^*} on the observed enhancements in j_{C2+} . Lastly, using the s-GDE design and a Cu/Fe-N-C tandem CL, 90% FE to C₂₊ products at a j_{C2+} exceeding 1 A cm⁻² and a half-cell energy efficiency for CO₂-to-C₂H₄ conversion of 40.1% was achieved. The s-GDE architecture employed in the present study presents unique opportunities for application in industrial systems for CO₂ electrolysis. Aside from the achievement of high C₂₊ current densities and FEs with a relatively low loading of Ag, the present study leverages along-the-channel gradients to enhance CO utilization in a tandem catalyst. These downstream concentration gradients will be more pronounced in industrial systems that employ larger electrodes for CO₂ reduction at scale. Therefore, it can be imagined that the developed s-GDE scheme would be even more effective at-scale, and future studies should aim to examine the performance of these s-GDEs within industrial scale electrolyzers and cell sizes and distinct flow channel architectures to enhance the readiness of the emerging technology.

Methods

Multiphysics simulation. The simulation was performed using the COMSOL Multiphysics

5.6 software package. The Navier-Stokes equations were used to solve the bulk fluid transport within the flow channel. Darcy's Law described the flow of fluid through a porous medium. The concentration of species was solved in throughout the domain by solving species conservation, and the θ_{*CO} was defined by the Langmuir adsorption model. **Supplementary Methods** provide more detailed information regarding the simulations.

Preparation of the segmented gas-diffusion electrode. The Cu catalyst ink was prepared by dispersing 200 mg of Cu nanoparticles (25 nm, MilliporeSigma) in a solvent mixture followed by ultrasonication for 30 minutes. The solvent mixture is comprised of 20 mL water, 20 mL isopropyl alcohol, and 500 μ L Sustainion XA-9 ionomer solution (5 wt.%). The Ag (20-40 nm, Alfa Aesar), ZnO (< 100 nm, MilliporeSigma), and Fe-N-C catalyst inks were prepared using the same procedure. The volume of solvent and ionomer solution was adjusted in proportion to the catalyst weight. The Cu catalyst ink was firstly sprayed onto the 8.0×25.0 cm² gas diffusion layer (GDL, Sigracet 39BC) to fabricate a uniform Cu GDE. The actual loading of Cu catalyst was 0.40 mg cm⁻² unless otherwise stated. The catalyst loading was determined by weighing the electrode before and after the spraying. This Cu GDE was then cut into four equal pieces (2.0×25.0 cm²). Three of them were used for subsequent coating with CO-selective catalyst inks, while the fourth piece was used as a control electrode.

The Cu GDE was then covered by various templates made of polyethylene terephthalate plastic. The templates were machined to open windows with different lengths of 0.10, 0.20, 0.40, 0.80, 1.20, 1.60, and 1.90 cm. Afterward, the Ag catalyst ink was sprayed onto the Cu CL to form an Ag CL segment with a constrained area at one end of the electrode. The mass of Ag catalyst was fixed to 0.04 mg for each 1.0 cm² stacked s-GDE. The quantity was determined by weighing a large piece of the electrode before and after the spraying. The templates with lengths of 1.0 mm and 19.0 mm were used together to fabricate the co-planar Cu/Ag s-GDE. The mass of Cu and Ag catalyst in each 1.0 cm² co-planar Cu/Ag s-GDE is also 0.40 and 0.04 mg, respectively. Following spraying, the s-GDEs were dried at 60 °C in the vacuum oven. Finally, the big sheet of stacked s-GDE was cut into smaller samples with dimensions of 2.00 cm (length, L) \times 0.50 cm (width, W) corresponding to an area of 1.00 cm² for the electrochemical tests. For the co-planar Cu/Ag s-GDE, the Cu and Ag CLs had the same width of 0.50 cm, and the segment areas were 0.95 and 0.05 cm² for Cu and Ag CLs, respectively. The Cu/Ag (1.00:1.00) s-GDE, which has an equal area of 1.00 cm² for Cu and Ag CLs segments, is equivalent to the l-GDE. The Cu/ZnO and Cu/Fe-N-C s-GDEs were fabricated by following the same procedure. The doubly loaded Cu/Fe-N-C s-GDE contained a Cu loading of 0.80 mg cm⁻² and Fe-N-C mass of around 0.08 mg for each 1.0 cm² electrode.

Preparation of modified s-GDEs. To prepare the modified s-GDEs, the uniform Cu CL (0.40 mg cm⁻²) segment (2.00 (L) \times 0.50 (W) cm²) was first coated onto the GDL, followed by a condensed Ag CL segment (0.20 (L) \times 0.50 (W) cm²) at the inlet. The amount of Ag catalyst (0.04 mg for each 1.0 cm² electrode) was kept the same for all electrodes. The area and position

of the Ag CL segment were precisely controlled by a machined template. Afterward, a sub-segment of the Cu CL with length varying from 0 to 1.80 cm was exfoliated off the GDL by 3M Magic tape until the microporous layer of black carbon was entirely exposed. The exposed GDL was then sealed by epoxy to prevent the undesired hydrogen evolution reaction from occurring on the carbon (**Supplementary Figure S31**). The backside of the exposed carbon paper was sealed as well to prevent the gas from diffusing into the carbon paper in the exfoliated area.

Preparation of Fe-N-C catalyst. The Fe-N-C catalyst was synthesized according to our previous report.⁴⁷ Briefly, 1 g of the PBX 51 powder (Cabot Corporation) was oxidized by the oxygen plasma and then dispersed in 100 mL of 5 mg mL⁻¹ ferric chloride hexahydrate (MilliporeSigma) solution. After sonicating for 2 h followed by stirring for 12 h, the precipitate was collected by centrifuging and dried in the oven overnight. Next, 100 mg of the carbon substrate was ground together with 300 mg of dicyandiamide and pyrolyzed in the tube furnace at 650 °C for 2 h under the N₂ stream. The obtained black powder was then washed in 1 M HNO₃ for 12 h. Finally, after drying the powder in the oven overnight, the Fe-N-C catalyst was ready to use.

Electrode characterization. The cross-sectional area of the electrode was imaged by scanning electron microscopy (SEM, FEI SCIOS DualBeam). The SEM samples were prepared by breaking the electrodes in the liquid N₂. The optical images of electrodes were taken by optical microscopes (Keyence VHX-2000E).

The electrochemically active surface area was determined by measuring the double-layer capacitance (C_{dl}) of the corresponding electrodes in Ar-purged 1.0 M KOH in a H-type electrolyzer. To exclude the effect of carbon paper, the backside of the electrode was sealed with epoxy and only left the CL exposed. The scan rate varied from 10 to 100 mV s⁻¹ in the non-Faradaic potential range. The obtained current was plotted as a function of the scan rate to derive the C_{dl} .

CO₂ electrochemical reduction in the MEA electrolyzer. The activity and selectivity of both s-GDE and l-GDE were tested in a customized MEA electrolyzer comprising the GDE cathode, Sustainion anion exchange membrane, and the Ni-Fe LDH coated Ni foam as the anode. The 0.50 M KOH or 0.10 M KHCO₃ anolyte stream that flowed through the anode at a rate of 5.00 mL min⁻¹ was controlled by a peristaltic pump (Harvard Apparatus P70-7000). The dry CO₂ feedstock was supplied to the cathode at a rate of 20 sccm controlled by a mass flow controller (Alicat Scientific MC-100SCCM-D). The applied cell voltage was controlled by a potentiostatic/galvanostatic station (Solartron EnergyLab XM). The anode potential was monitored online in reference to a saturated calomel electrode (SCE). The gas products were quantified by gas chromatography (GC, Agilent 7890B), while liquid products were measured by ¹H nuclear magnetic resonance spectroscopy (Bruker AV500).

The FE of each gas product was calculated based on a prior equation where the outlet CO₂ flow rate was accurately measured.²⁹ For the measurement of outlet CO₂ flow rate, a constant stream of Ar gas (10 sccm) was used as an internal reference and evenly mixed with the cell outlet gas stream before it was injected into the GC column. The standard curve for CO₂ flow rate was established by a similar way of mixing the 10 sccm Ar gas with a pure CO₂ stream with a flow rate varying from 5 to 100 sccm. The concentration of other gas components was quantified by using CO₂ as the internal reference. The standard GC calibration curves for the other gas components were established based on three standard calibration gases, comprising 1000, 2000, and 5000 ppm of H₂, CO, CH₄, C₂H₄, and C₂H₆, respectively, with CO₂ as the balance gas.

The internal ohmic resistance between the cathode and anode was determined by electrochemical impedance spectroscopy operated under open-circuit voltage with a frequency ranging from 10⁵ Hz to 0.01 Hz. Almost 90% of the measured cell resistances ranged from 0.20 to 0.30 Ω, while around 10% of cell resistance ranged from 0.50 to 0.60 Ω. Contact resistances resulting from cell assembly contributes 0.10 Ω variance whereas variations in the membrane ion conductivity from batch to batch accounts for another 0.30 Ω variance. Therefore, to deconvolute the impacts of these variances from the kinetic performance, the cell voltage was IR compensated unless otherwise stated. All the reported cell voltages were corrected by the measured cell internal resistance loss under each specific test unless otherwise stated. For the modified s-GDEs, the cathode potential was obtained by subtracting the recorded anode potential from IR-free cell voltage.

The full-cell energy efficiency for a specific product *i* was assessed according to

$$EE_{i,full-cell}(\%) = \frac{E_i^0}{V_{cell}} \times FE_i(\%)$$

Where E_i^0 is the equilibrium cell voltage ($E_i^0 = E_{anode}^0 - E_{i,cathode}^0$) for a specific product *i*; V_{cell} is the applied cell voltage; FE_i is the Faradaic efficiency of product *i*.

The half-cell energy efficiency for a specific product *i* was calculated by the following equation:

$$EE_{i,half-cell}(\%) = \frac{E_i^0}{E_{anode}^0 - E_{cathode}} \times FE_i(\%)$$

Where $E_{cathode}$ is the applied cathode potential.

CO₂ reduction in the flow cell. The flow cell, including a 2 mm buffer layer of catholyte (0.5 M KOH), has a larger ohmic resistance (1.00 to 1.10 Ω) than that for the MEA electrolyzer. The test conditions in the flow cell were generally identical to those in the MEA electrolyzer except that a catholyte was supplied at a flow rate of 0.5 mL min⁻¹.

Long-term stability test in the MEA electrolyzer and flow cell. The long-term stability was operated under potentiostatic mode in which the cell voltage was controlled by the Solartron EnergyLab XM. During the long-term testing, gas and liquid products were periodically quantified by GC and ^1H NMR, respectively.

Calculation of the CO_2 reduction performance on each sub-segment. The Cu CL sub-segment (S_i) as shown in **Figure 3e** was defined as the difference in Cu CL segments between two consecutive modified s-GDEs (E_i) as follows:

$$S_1 = E_1; S_i = E_i - E_{i-1}, (6 \geq i \geq 2)$$

where i is an integer. Correspondingly, the $j_{\text{C}_{2+}}$ for each sub-segment was calculated by finding the total current in each sub-segment and dividing by the sub-segment area as follows:

$$j_{\text{C}_{2+}}(S_1) = \frac{I_{\text{C}_{2+}}(E_1)}{A(E_1)}; j_{\text{C}_{2+}}(S_i) = \frac{I_{\text{C}_{2+}}(E_i) - I_{\text{C}_{2+}}(E_{i-1})}{A(E_i) - A(E_{i-1})}, (6 \geq i \geq 2)$$

In this equation, $I_{\text{C}_{2+}}(E_i)$ is the total C_{2+} current (units of mA) in segment E_i , $A(E_i)$ is the area of segment E_i . and $j_{\text{C}_{2+}}(S_i)$ is the C_{2+} current density (units of mA cm^{-2}) in sub-segment S_i .

Calculation of the outlet CO flow rate from each sub-segment. The outlet CO flow rate for each S_i was directly converted from the I_{CO} for the corresponding E_i according to the following equation.

$$Q_{\text{CO}}(S_i) = \frac{I_{\text{CO}}(E_i)}{nF}$$

where the Q_{CO} (mol s^{-1}) represents the flow rate of CO along the y-axis of the electrode within a given sub-segment, the n is the number of electron transfer ($n = 2$), and the F is Faraday's constant.

Calculation of CO_2 crossover

This work applied an Ar stream with a constant flow rate as an internal standard to calibrate the CO_2 flow rate; so that the CO_2 flow rate at the outlet can be accurately measured, as shown below.

$$\frac{Q_{\text{CO}_2}}{Q_{\text{Ar}}} = a \times \frac{A_{\text{CO}_2}}{A_{\text{Ar}}} + b$$

where the Q_{CO_2} and Q_{Ar} are the volumetric flow rate of CO_2 and Ar, while the Q_{Ar} is 10.00 sccm; the A_{CO_2} and A_{Ar} represent the peak area of CO_2 and Ar in the GC trace; the a and b are the slope and intercept of the calibration curve, respectively.

The difference in CO_2 flow rate between the inlet and outlet accounts for the CO_2 consumption

and the CO₂ crossover to the anode side. The volumetric rate of CO₂ (\dot{V}) consumed by the Faradaic reaction can be calculated from the current.

$$\dot{V}_{consumption} = \frac{\sum \frac{I_i}{n_i * F} \times R \times T}{P}$$

where the n is the number of charge transfer for product i; F is the Faradaic constant; R is the gas constant; P is the gas pressure; T is the temperature.

Therefore, the volume of CO₂ crossover can be calculated as follows.

$$\dot{V}_{crossover} = \dot{V}_{inlet} - \dot{V}_{outlet} - \dot{V}_{consumption}$$

Author contributions

J.W., A.Z.W., and A.T.B. supervised the project. J.W. and T.Z. designed the experiments. T.Z. prepared the electrodes, performed electrochemical experiments and characterizations. with the help of Z.L. J.C.B. performed multiphysics simulation. T.Z., Z.L., and J.C.B. performed data interpretation. T.Z., J.C.B., A.T.B., A.Z.W, and J.W. wrote the manuscript. All authors discussed, commented on, and revised the manuscript.

Correspondence and requests for materials should be addressed to Jingjie Wu and Adam Z. Weber.

Acknowledgements

This material is based upon work supported by the Office of Fossil Energy and Carbon Management of the U.S. Department of Energy under Award Number DE-FE0031919 and performed at the Joint Center for Artificial Photosynthesis, a DOE Energy Innovation Hub, supported through the Office of Science of the U.S. Department of Energy under Award Number DE-SC0004993 and the National Institutes of Health under Grant No. S10OD023532. The authors at University of Cincinnati also thank National Science Foundation for financial support (Award No. CBET-2033343). JCB acknowledges funding from the National Science Foundation Graduate Research Fellowship under Grant No. DGE 1752814. JCB would also like to acknowledge fruitful discussion regarding along-the-channel transport in CO₂ electrolyzers with Eric Lees.

References

- 1 Jouny, M., Luc, W. W. & Jiao, F. A General Techno-Economic Analysis of CO₂ Electrolysis Systems. *Industrial & Engineering Chemistry Research*, doi:10.1021/acs.iecr.7b03514 (2018).
- 2 Nitopi, S. *et al.* Progress and Perspectives of Electrochemical CO₂ Reduction on Copper in Aqueous Electrolyte. *Chem Rev* **119**, 7610-7672, doi:10.1021/acs.chemrev.8b00705 (2019).
- 3 Dinh, C.-T. *et al.* CO₂ electroreduction to ethylene via hydroxide-mediated copper catalysis at an abrupt interface. *Science* **360**, 783-787, doi:10.1126/science.aas9100 (2018).
- 4 Gao, Y. *et al.* Recent Advances in Intensified Ethylene Production—A Review. *ACS Catalysis* **9**, 8592-8621, doi:10.1021/acscatal.9b02922 (2019).
- 5 Montoya, J. H., Peterson, A. A. & Nørskov, J. K. Insights into C-C Coupling in CO₂ Electroreduction on Copper Electrodes. *ChemCatChem* **5**, 737-742, doi:10.1002/cctc.201200564 (2013).
- 6 Montoya, J. H., Shi, C., Chan, K. & Nørskov, J. K. Theoretical Insights into a CO Dimerization Mechanism in CO₂ Electroreduction. *J Phys Chem Lett* **6**, 2032-2037, doi:10.1021/acs.jpcllett.5b00722 (2015).
- 7 Schouten, K. J. P., Kwon, Y., van der Ham, C. J. M., Qin, Z. & Koper, M. T. M. A new mechanism for the selectivity to C₁ and C₂ species in the electrochemical reduction of carbon dioxide on copper electrodes. *Chemical Science* **2**, doi:10.1039/c1sc00277e (2011).
- 8 Schouten, K. J. P., Pérez Gallent, E. & Koper, M. T. M. Structure Sensitivity of the Electrochemical Reduction of Carbon Monoxide on Copper Single Crystals. *ACS Catalysis* **3**, 1292-1295, doi:10.1021/cs4002404 (2013).
- 9 Liu, X. *et al.* pH effects on the electrochemical reduction of CO₂ towards C₂ products on stepped copper. *Nat Commun* **10**, 32, doi:10.1038/s41467-018-07970-9 (2019).
- 10 Garza, A. J., Bell, A. T. & Head-Gordon, M. Mechanism of CO₂ Reduction at Copper Surfaces: Pathways to C₂ Products. *ACS Catalysis*, 1490-1499, doi:10.1021/acscatal.7b03477 (2018).
- 11 Resasco, J. *et al.* Promoter Effects of Alkali Metal Cations on the Electrochemical Reduction of Carbon Dioxide. *J Am Chem Soc* **139**, 11277-11287, doi:10.1021/jacs.7b06765 (2017).
- 12 Li, J. *et al.* Constraining CO coverage on copper promotes high-efficiency ethylene electroproduction. *Nature Catalysis*, doi:10.1038/s41929-019-0380-x (2019).
- 13 Choi, C. *et al.* Highly active and stable stepped Cu surface for enhanced electrochemical CO₂ reduction to C₂H₄. *Nature Catalysis* **3**, 804-812, doi:10.1038/s41929-020-00504-x (2020).
- 14 Gu, Z. *et al.* Efficient Electrocatalytic CO₂ Reduction to C₂+ Alcohols at Defect-Site-Rich Cu Surface. *Joule*, doi:10.1016/j.joule.2020.12.011 (2021).
- 15 Zhong, M. *et al.* Accelerated discovery of CO₂ electrocatalysts using active machine learning. *Nature* **581**, 178-183, doi:10.1038/s41586-020-2242-8 (2020).
- 16 Vasileff, A., Xu, C., Jiao, Y., Zheng, Y. & Qiao, S.-Z. Surface and interface engineering in copper-based bimetallic materials for selective CO₂ electroreduction. *Chem* **4**, 1809-1831 (2018).
- 17 Huang, Y., Handoko, A. D., Hirunsit, P. & Yeo, B. S. Electrochemical reduction of CO₂ using copper single-crystal surfaces: Effects of CO* coverage on the selective formation of ethylene. *ACS Catalysis* **7**, 1749-1756 (2017).
- 18 Monzó, J. *et al.* Enhanced electrocatalytic activity of Au-Cu core-shell nanoparticles

- towards CO₂ reduction. *Journal of Materials Chemistry A* **3**, 23690-23698, doi:10.1039/c5ta06804e (2015).
- 19 Morales-Guio, C. G. *et al.* Improved CO₂ reduction activity towards C₂+ alcohols on a tandem gold on copper electrocatalyst. *Nature Catalysis* **1**, 764-771, doi:10.1038/s41929-018-0139-9 (2018).
 - 20 Chen, C. *et al.* Cu-Ag Tandem Catalysts for High-Rate CO₂ Electrolysis toward Multicarbon. *Joule* **4**, 1688-1699, doi:10.1016/j.joule.2020.07.009 (2020).
 - 21 Wang, X. *et al.* Mechanistic reaction pathways of enhanced ethylene yields during electroreduction of CO₂-CO co-feeds on Cu and Cu-tandem electrocatalysts. *Nature Nanotechnology*, doi:10.1038/s41565-019-0551-6 (2019).
 - 22 Gao, J. *et al.* Selective C-C Coupling in Carbon Dioxide Electroreduction via Efficient Spillover of Intermediates As Supported by Operando Raman Spectroscopy. *J Am Chem Soc* **141**, 18704-18714, doi:10.1021/jacs.9b07415 (2019).
 - 23 Fu, J. *et al.* Bipyridine-assisted assembly of Au nanoparticles on Cu nanowires to enhance electrochemical reduction of CO₂. *Angewandte Chemie International Edition* (2019).
 - 24 Hoang, T. T. H. *et al.* Nanoporous Copper-Silver Alloys by Additive-Controlled Electrodeposition for the Selective Electroreduction of CO₂ to Ethylene and Ethanol. *J Am Chem Soc* **140**, 5791-5797, doi:10.1021/jacs.8b01868 (2018).
 - 25 Li, F. *et al.* Cooperative CO₂-to-ethanol conversion via enriched intermediates at molecule-metal catalyst interfaces. *Nature Catalysis* **3**, 75-82, doi:10.1038/s41929-019-0383-7 (2019).
 - 26 Wang, L. *et al.* Electrochemical Carbon Monoxide Reduction on Polycrystalline Copper: Effects of Potential, Pressure, and pH on Selectivity toward Multicarbon and Oxygenated Products. *ACS Catalysis* **8**, 7445-7454, doi:10.1021/acscatal.8b01200 (2018).
 - 27 Schreier, M., Yoon, Y., Jackson, M. N. & Surendranath, Y. Competition between H and CO for Active Sites Governs Copper-Mediated Electrosynthesis of Hydrocarbon Fuels. *Angew Chem Int Ed Engl* **57**, 10221-10225, doi:10.1002/anie.201806051 (2018).
 - 28 Ren, D. *et al.* Atomic Layer Deposition of ZnO on CuO Enables Selective and Efficient Electroreduction of Carbon Dioxide to Liquid Fuels. *Angewandte Chemie International Edition* **58**, 15036-15040 (2019).
 - 29 She, X. *et al.* Tandem Electrodes for Carbon Dioxide Reduction into C₂+ Products at Simultaneously High Production Efficiency and Rate. *Cell Reports Physical Science* **1**, doi:10.1016/j.xcrp.2020.100051 (2020).
 - 30 Zhang, T., Li, Z., Zhang, J. & Wu, J. Enhance CO₂-to-C₂+ products yield through spatial management of CO transport in Cu/ZnO tandem electrodes. *Journal of Catalysis*, doi:10.1016/j.jcat.2020.05.002 (2020).
 - 31 Levenspiel, O. *Chemical reaction engineering*. (John Wiley & Sons, 1999).
 - 32 Weng, L.-C., Bell, A. T. & Weber, A. Z. A systematic analysis of Cu-based membrane-electrode assemblies for CO₂ reduction through multiphysics simulation. *Energy & Environmental Science*, doi:10.1039/d0ee01604g (2020).
 - 33 Kas, R. *et al.* Along the Channel Gradients Impact on the Spatioactivity of Gas Diffusion Electrodes at High Conversions during CO₂ Electroreduction. *ACS Sustainable Chemistry & Engineering* **9**, 1286-1296 (2021).
 - 34 Bui, J. C., Kim, C., Weber, A. Z. & Bell, A. T. Dynamic Boundary Layer Simulation of Pulsed CO₂ Electrolysis on a Copper Catalyst. *ACS Energy Letters*, 1181-1188, doi:10.1021/acsenenergylett.1c00364 (2021).
 - 35 Dunwell, M., Luc, W., Yan, Y., Jiao, F. & Xu, B. Understanding Surface-Mediated Electrochemical Reactions: CO₂ Reduction and Beyond. *ACS Catalysis*, 8121-8129,

- doi:10.1021/acscatal.8b02181 (2018).
- 36 Moradzaman, M., Martínez, C. S. & Mul, G. Effect of partial pressure on product selectivity in Cu-catalyzed electrochemical reduction of CO₂. *Sustainable Energy & Fuels* **4**, 5195-5202, doi:10.1039/d0se00865f (2020).
 - 37 Hori, Y., Takahashi, R., Yoshinami, Y. & Murata, A. Electrochemical reduction of CO at a copper electrode. *The Journal of Physical Chemistry B* **101**, 7075-7081 (1997).
 - 38 Wang, L. *et al.* Selective reduction of CO to acetaldehyde with CuAg electrocatalysts. *Proc Natl Acad Sci U S A* **117**, 12572-12575, doi:10.1073/pnas.1821683117 (2020).
 - 39 Corral, D. *et al.* Advanced manufacturing for electrosynthesis of fuels and chemicals from CO₂. *Energy & Environmental Science*, doi:10.1039/d0ee03679j (2021).
 - 40 Tan, Y. C., Lee, K. B., Song, H. & Oh, J. Modulating Local CO₂ Concentration as a General Strategy for Enhancing C–C Coupling in CO₂ Electroreduction. *Joule* **4**, 1104-1120, doi:10.1016/j.joule.2020.03.013 (2020).
 - 41 Salvatore, D. A. *et al.* Electrolysis of Gaseous CO₂ to CO in a Flow Cell with a Bipolar Membrane. *ACS Energy Letters* **3**, 149-154, doi:10.1021/acsenenergylett.7b01017 (2017).
 - 42 Chen, Y. *et al.* A Robust, Scalable Platform for the Electrochemical Conversion of CO₂ to Formate: Identifying Pathways to Higher Energy Efficiencies. *ACS Energy Letters* **5**, 1825-1833, doi:10.1021/acsenenergylett.0c00860 (2020).
 - 43 Huang, J. E. *et al.* CO₂ electrolysis to multicarbon products in strong acid. *Science* **372**, 1074-1078 (2021).
 - 44 McCallum, C. *et al.* Reducing the crossover of carbonate and liquid products during carbon dioxide electroreduction. *Cell Reports Physical Science*, doi:10.1016/j.xcrp.2021.100522 (2021).
 - 45 Li, T. *et al.* Electrolytic Conversion of Bicarbonate into CO in a Flow Cell. *Joule* **3**, 1487-1497, doi:10.1016/j.joule.2019.05.021 (2019).
 - 46 Weng, L.-C., Bell, A. T. & Weber, A. Z. Towards membrane-electrode assembly systems for CO₂ reduction: a modeling study. *Energ Environ Sci* **12**, 1950-1968, doi:10.1039/c9ee00909d (2019).
 - 47 Zhang, T. *et al.* Nickel-nitrogen-carbon molecular catalysts for high rate CO₂ electroreduction to CO: on the role of carbon substrate and reaction chemistry. *ACS Applied Energy Materials* (2020).

Highly Selective and Productive Reduction of Carbon Dioxide to Multicarbon Products via in-situ CO Management using Segmented Tandem Electrodes

Tianyu Zhang¹⁺, Justin C. Bui^{2,3+}, Zhengyuan Li¹, Alexis T. Bell^{2,3}, Adam Z. Weber^{3*}, Jingjie Wu^{1*}

¹Department of Chemical and Environmental Engineering, University of Cincinnati, Cincinnati, OH, 45221, United States

²Department of Chemical and Biomolecular Engineering, University of California Berkeley, Berkeley, CA, 94720, United States

³Joint Center for Artificial Photosynthesis, Lawrence Berkeley National Laboratory, Berkeley, CA, 94720, United States

⁺These authors contributed equally

^{*}Corresponding authors: azweber@lbl.gov; jingjie.wu@uc.edu

Supplementary Methods

Multiphysics simulation model description. Transport of CO₂ and CO within the cathode compartment of an AEM CO₂ electrolyzer employing a segmented gas-diffusion electrode (s-GDE) was modeled in two-dimensions under steady-state conditions for measured total current densities of 200, 300, 400, 500, 600, and 700 mA cm⁻² for various Cu:Ag area ratios from 1.00:0.05 to 1.00:1.00. The following section describes the modeling approach and the simplifying assumptions made regarding electrochemical kinetics and transport within the simulation. A schematic of the simulated s-GDE geometry is shown in **Supplementary Figure 1**. Three domains are illustrated – the Cu catalyst layer (Cu CL), the gas-diffusion layer (GDL), and the gas channel (Channel). The modeled domain is denoted by the dashed red outline in **Supplementary Figure 1**. It is important to note that the anion-exchange membrane (AEM) and the Ag CL are treated as boundary elements and not fully modeled. Pure gas-phase CO₂ is fed from the top of the 1-mm-wide gas channel at a flow rate of 20 sccm. The GDL has a thickness of 325 μm, as reported by Sigracet.¹ The Cu CL has a thickness of 2 μm. The length of the flow channel is 2 cm. Constant pressure, laminar flow in the gas channel was modeled using the Navier-Stokes equation as described by Kas *et al.*² Gas-phase transport through the porous GDL and Cu CL was modeled using Darcy's Law. Species conservation of CO₂, CO, and N₂ was maintained in all domains.

Transport in gas channel. The transport of CO, CO₂, and N₂ in the gas channels is driven by convection and diffusion. The convective flow velocity and pressure gradient were calculated by solving the Navier-Stokes equations, and diffusion was modeled using a mixture-average approach. The flux of species *i* (*N_i*) is given as follows,

$$N_i = \frac{1}{M_i} \left(-\rho_G D_i^{eff} \nabla \omega_i - \frac{\rho_G D_i^{eff} \omega_i \nabla M_A}{M_A} + \rho_i \mathbf{u}_G \right) \quad (S1)$$

where *M_i* is the molar mass of species *i*; *ω_i* is the mole fraction of species *i*; *D_i^{eff}* is the effective diffusion coefficient of species *i*. $M_A = \left(\sum \frac{\omega_i}{M_i} \right)^{-1}$ is the average molecular weight of the mixture. *ρ_G* is the density of the gaseous mixture and *u_G* is the convective velocity of the gaseous mixture.

The diffusivity, *D_i^{eff}*, is given by the following equation,

$$D_i^{eff} = \frac{1 - \omega_i}{\sum_{i \neq k} \frac{x_k}{D_{ik}}} \quad (S2)$$

where *D_{ik}* is a binary diffusivity of species *i* and species *k*.

The Navier-Stokes equations were used to solve for the convective velocity, \mathbf{u}_g , and can be written as the continuity equation,

$$\nabla \cdot (\rho_g \mathbf{u}_g) = 0 \quad (\text{S3})$$

and the momentum balance in the absence of external body forces,

$$\rho_g (\mathbf{u}_g \cdot \nabla \mathbf{u}_g) = \nabla p + \mu_g (\nabla \mathbf{u}_g + (\nabla \mathbf{u}_g)^T) - \frac{2}{3} \mu (\nabla \cdot \mathbf{u}_g) \mathbf{I} \quad (\text{S4})$$

where μ_g is the mixture viscosity, p is the pressure, and \mathbf{I} is the identity matrix. Parameters employed for the model are given in **Supplementary Table S1**.

There are no reactions within the channel. Therefore, the species conservation equation can be written as follows.

$$\nabla \cdot N_i = 0 \quad (\text{S5})$$

Boundary conditions for the channel domain include the following. The gas-phase at the inlet of the channel was 100 % CO₂, moving with a linear velocity of $\mathbf{u}_g = 0.33 \frac{\text{m}}{\text{s}}$. An open boundary condition was assumed at the outlet (i.e., the atmospheric pressure is equivalent to the normal stress), with a fixed pressure equivalent to atmospheric pressure, $p_{out} = 1 \text{ atm}$. At the wall of the channel, a no flux condition was assumed for all species; no-slip and no penetration conditions were imposed for the fluid velocity.

Transport in GDL and Cu CL. The transport of CO, CO₂, and N₂ in the GDL is nearly identical to that in the channel:

$$N_i = \frac{1}{M_i} \left(-\rho_g D_i^{eff} \nabla \omega_i - \frac{\rho_g D_i^{eff} \omega_i \nabla M_A}{M_A} + \rho_i \mathbf{u}_g \right) \quad (\text{S6})$$

However, to account for the porous nature of the GDL and Cu CL, the expression for the diffusivity of each species is corrected for the medium porosity (ε_m) and tortuosity (τ_m) as follows:

$$D_i^{eff} = \frac{D_i \varepsilon_m}{\tau_m} \quad (\text{S7})$$

where $\tau_m = \varepsilon_m^{-\frac{1}{2}}$ through the Bruggeman relationship.

The convective velocity and pressure were calculated using Darcy's Law,

$$\mathbf{u}_g = \frac{\kappa_m}{\mu_g} \nabla p \quad (\text{S8})$$

where κ_m is the permeability of the porous medium.

For all wall boundaries, as well as at the Ag CL and AEM boundaries, no-slip and no penetration were taken as boundary conditions for Darcy's law.

No flux boundary conditions for all gaseous species were used at all boundaries except for the Ag CL boundary, where constant flux conditions were employed for CO and CO₂ as follows.

$$N_{CO,AgCL} = \frac{A_{Cu}}{A_{Ag}} \frac{j_{CO}}{n_{COER} F} \quad (S9)$$

$$N_{CO_2,AgCL} = -\frac{A_{Cu}}{A_{Ag}} \frac{j_{CO}}{n_{COER} F} \quad (S10)$$

where $\frac{A_{Cu}}{A_{Ag}}$ is the ratio of Cu CL area to Ag CL area and accounts for the local increase in Ag loading for higher Cu CL:Ag CL area ratios, n_{COER} is the number of electrons in the CO evolution reaction (COER), F is Faraday's constant, and j_{CO} is the current density for COER on the Ag, which is determined from the experimental polarization data.

Within the Cu CL, a coverage-dependent source term describes CO consumption to form CH₄ and C₂₊ products.

$$R_{CT,CO} = \theta_{*CO} \sum_k \frac{i_k n_{CO,k}}{A_v n_{e^-,k} F} \quad (S11)$$

where A_v is the surface area to volume ratio in the Cu CL, i_k is the volumetric partial current density for the formation of product k from CO determined from the experimental polarization data, $n_{CO,k}$ is the stoichiometry of CO in reaction k , and $n_{e^-,k}$ is the number of electron transfers for the formation of product k from CO.

θ_{*CO} is the local *CO coverage, defined through a first-order Langmuir adsorption model as follows,

$$\theta_{*CO} = \frac{P_{CO} K_{CO}}{1 + P_{CO} K_{CO}} \quad (S12)$$

where K_{CO} is the equilibrium coefficient for adsorption fit to a value of 10 atm⁻¹ from data collected by Li *et al.*³ for CO reduction in a vapor-phase CO electrolyzer at an applied potential of -0.3 V vs. RHE. The first-order dependence on CO partial pressure comes from multiple experimental and theoretical studies.³⁻⁶ While this first-order dependence could suggest a rate limiting step that occurs prior to C-C coupling, work by Wang *et al.* maintains that C-C coupling is indeed the rate limiting step and suggests that the first-order dependence at low partial pressure could be due to the heterogeneity of surface sites on Cu electrodes.⁵ Because step and kink sites will bind CO more strongly than terrace sites, competitive adsorption leads to CO coverage saturating more quickly at lower coverages on under-coordinated sites. Thus, at low partial pressure, the C₂₊ current density possesses reduced sensitivity to changes in CO

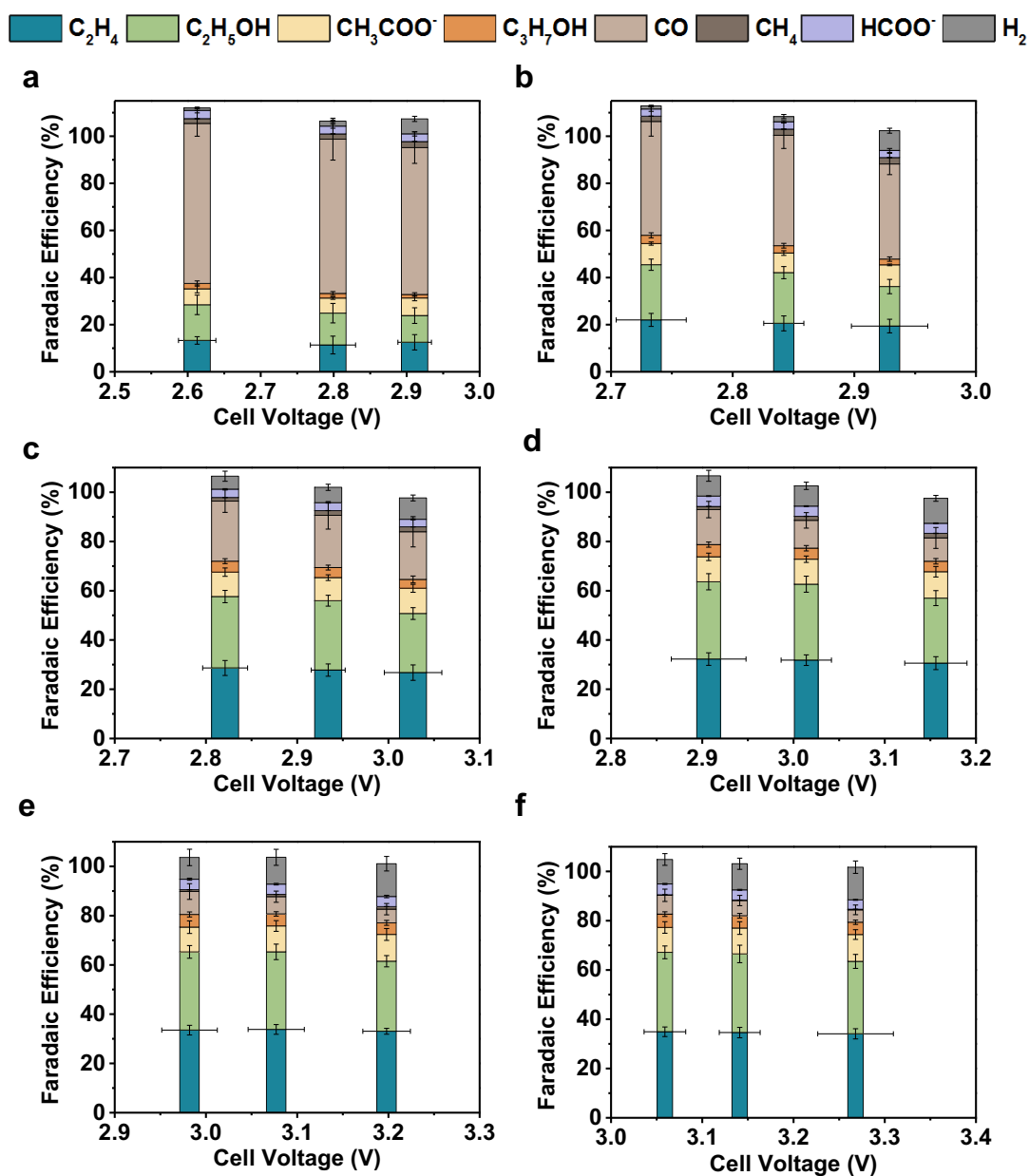
partial pressure than the second-order dependence implied by a C-C coupling rate limiting step.⁵ The fit and isotherm are shown below in **Supplementary Figure S2**.

The species conservation equation can be written as follows.

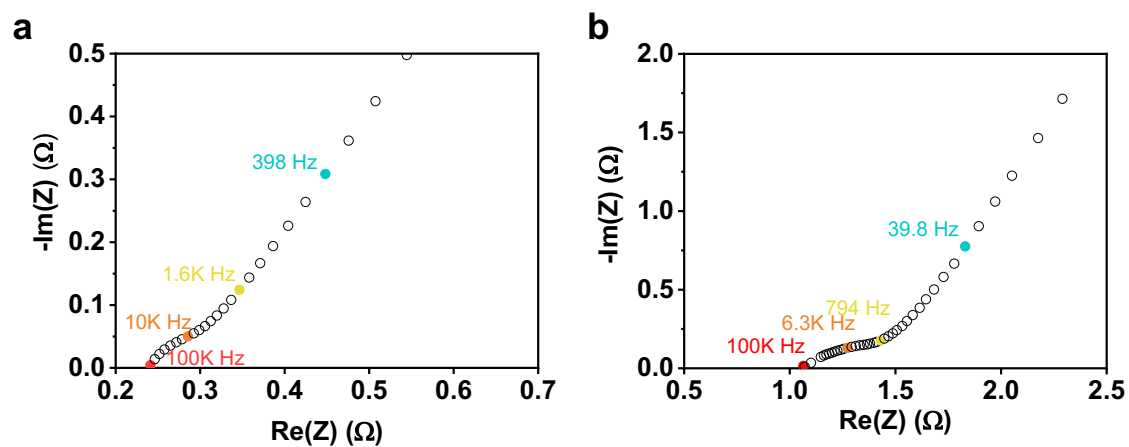
$$\nabla \cdot N_i = R_{CT,i} \quad (\text{S13})$$

It is important to note that a key assumption in the model is that the Cu/Ag catalyst behaves as a perfect tandem catalyst. In other words, all CO₂ is first converted to CO in the Ag CL, and that Ag-generated CO is then converted to CH₄ or C₂₊ products within the Cu CL. This assumption simplifies the complex kinetics of the tandem catalyst in the absence of an adequate microkinetic model to describe the complex dynamics of reagent and intermediate adsorption and is thus necessary to estimate local *CO coverages in the Cu CL. This assumption is supported by prior studies that have demonstrated that Ag is much more active for CO₂ reduction than Cu and that unmodified Cu has a poor activity for CO formation.⁷ Furthermore, the present model only accounts for gas-phase CO and CO₂ but neglects pH and ionic potential gradients and assumes equilibrium between the gas and ionomer phases within the CL. These gradients are likely significant, but their effects on the product distributions are difficult to capture without a complete microkinetic model, and their inclusion leads to problems with numerical convergence for the higher current densities achieved in the experimental work. Therefore, the effects of these factors have been neglected for this study. Nonetheless, while these assumptions likely cause a slight over-estimation of the achieved θ_{*CO} by assuming that all *CO is generated in the Ag CL and not solving for dissolution in the ionomer phase, they are likely adequate to examine the trend in θ_{*CO} across different Cu CL: Ag CL area ratios.

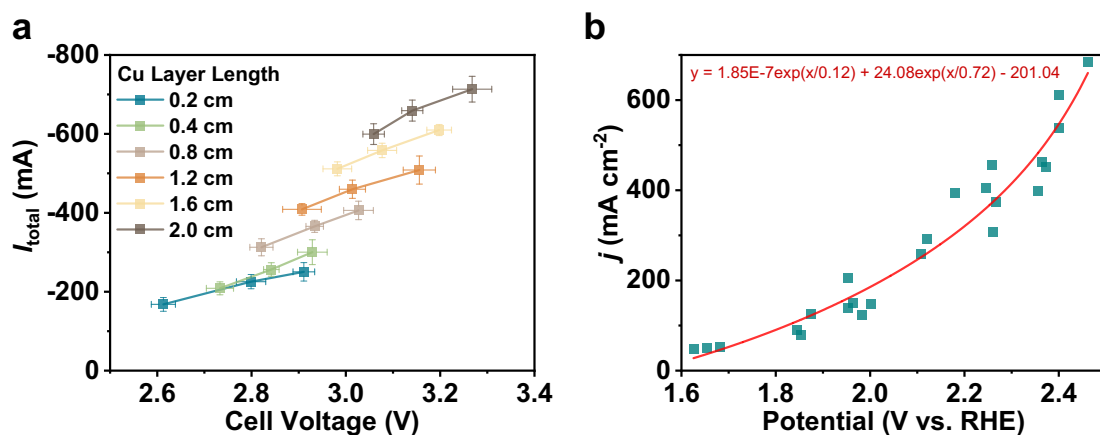
Computational methods. The governing equations (Navier-Stokes, Darcy's Law, and species conservation) were solved with the MUMPS general solver in COMSOL Multiphysics 5.6 using a relative tolerance of 0.001. The modeling domain was discretized with a 2-D nonuniform mesh consisting of 143130 domain elements and 12314 boundary elements.



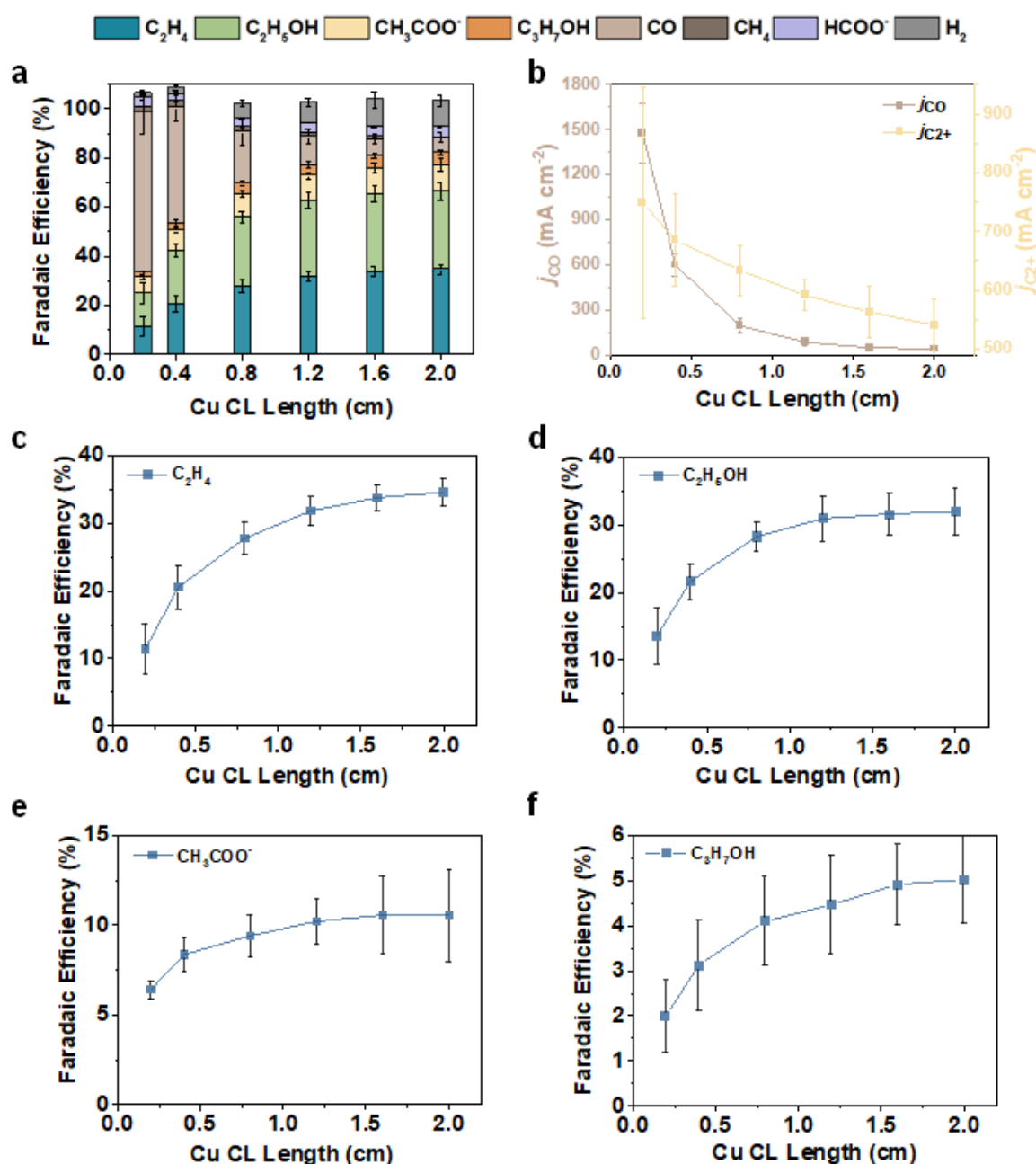
Supplementary Figure S1. Product distribution as a function of applied cell potential for the six modified Cu/Ag s-GDEs (from E₁ to E₆) with various Cu CL lengths of **(a)** 0.2 cm; **(b)** 0.4 cm; **(c)** 0.8 cm; **(d)** 1.2 cm; **(e)** 1.6 cm; **(f)** 2.0 cm. The cell voltage is IR corrected. The performance was measured in the MEA electrolyzer. The error bars represent the standard deviation of measurements from three independent electrodes.



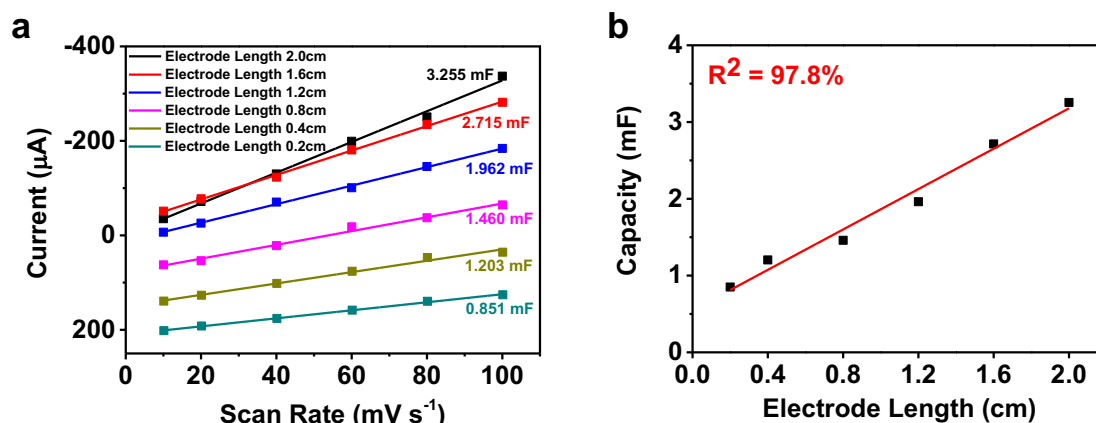
Supplementary Figure S2. Nyquist plots of the electrochemical impedance spectroscopy of **(a)** MEA electrolyzer and **(b)** flow cell with a thin buffer layer of 2 mm.



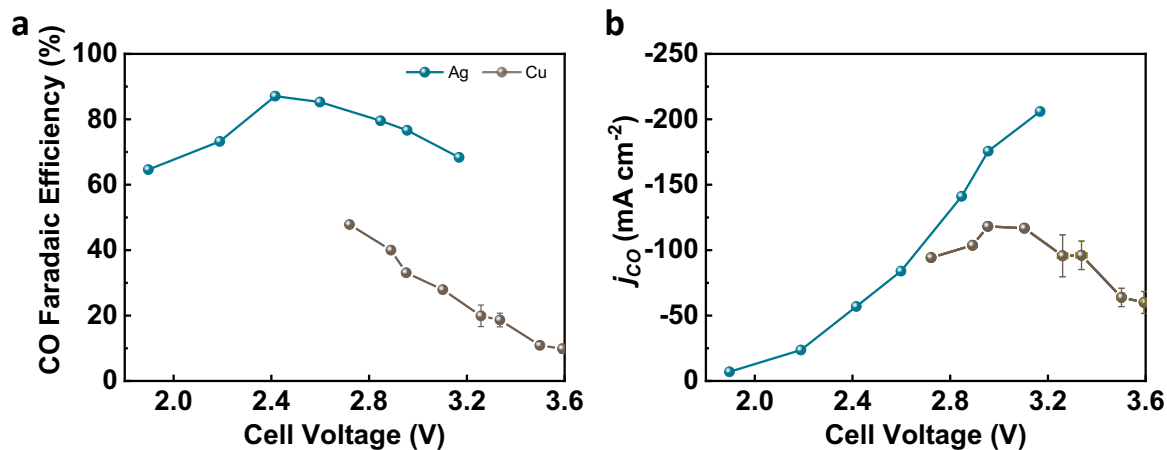
Supplementary Figure S3. (a) The total current of six modified Cu/Ag s-GDEs (from E₁ to E₆) with Cu CL lengths varying from 0.20 to 2.00 cm. **(b)** Polarization curve for the anodic reaction (oxygen evolution reaction, OER) on Ni-Fe-LDH. When the anode potential was obtained from the measured OER polarization curve at a certain current density, the cathode potential was calculated by subtracting the anode potential from IR-corrected cell voltage. In this way, we can convert the cell voltage in **Supplementary Figure S1** to cathode potential versus RHE. Subsequently, we compared the performance of six modified Cu/Ag s-GDEs at a similar cathode potential of -0.70 V vs. RHE in **Figure 2c and d** and **Supplementary Figure S4**.



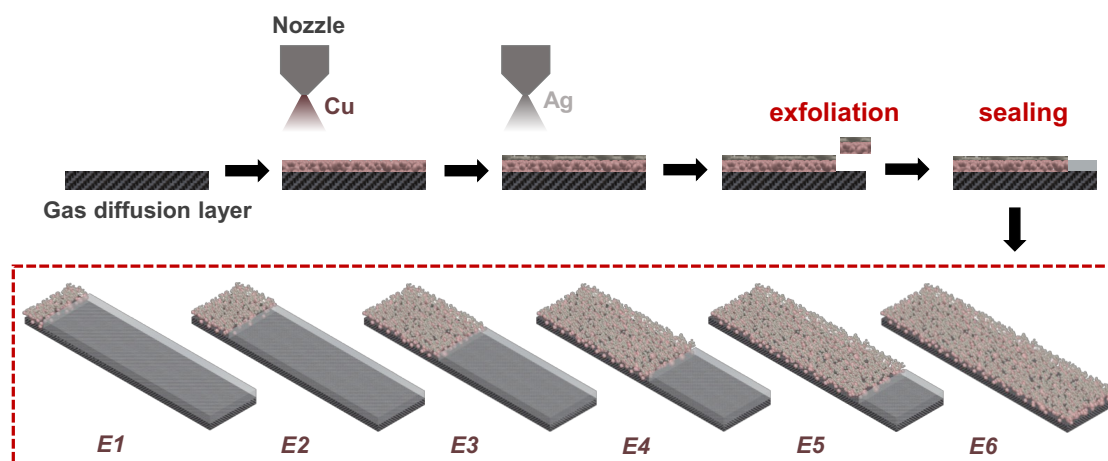
Supplementary Figure S4. (a) The product distribution and (b) the j_{CO} and j_{C2+} under the cathode potential of -0.7 V vs. RHE against the Cu CL length on the six modified Cu/Ag s-GDEs (from E₁ to E₆) with Cu CL length varying from 0.20 to 2.00 cm. The cathode potential was calculated by subtracting the measured anode potential from the IR-corrected applied cell voltage. (c-f) FE of representative C_{2+} products, (c) C_2H_4 , (d) C_2H_5OH , (e) CH_3COO^- , and (f) C_3H_7OH versus the Cu CL length at -0.7 V. The error bars represent the standard deviation of measurements from three independent electrodes.



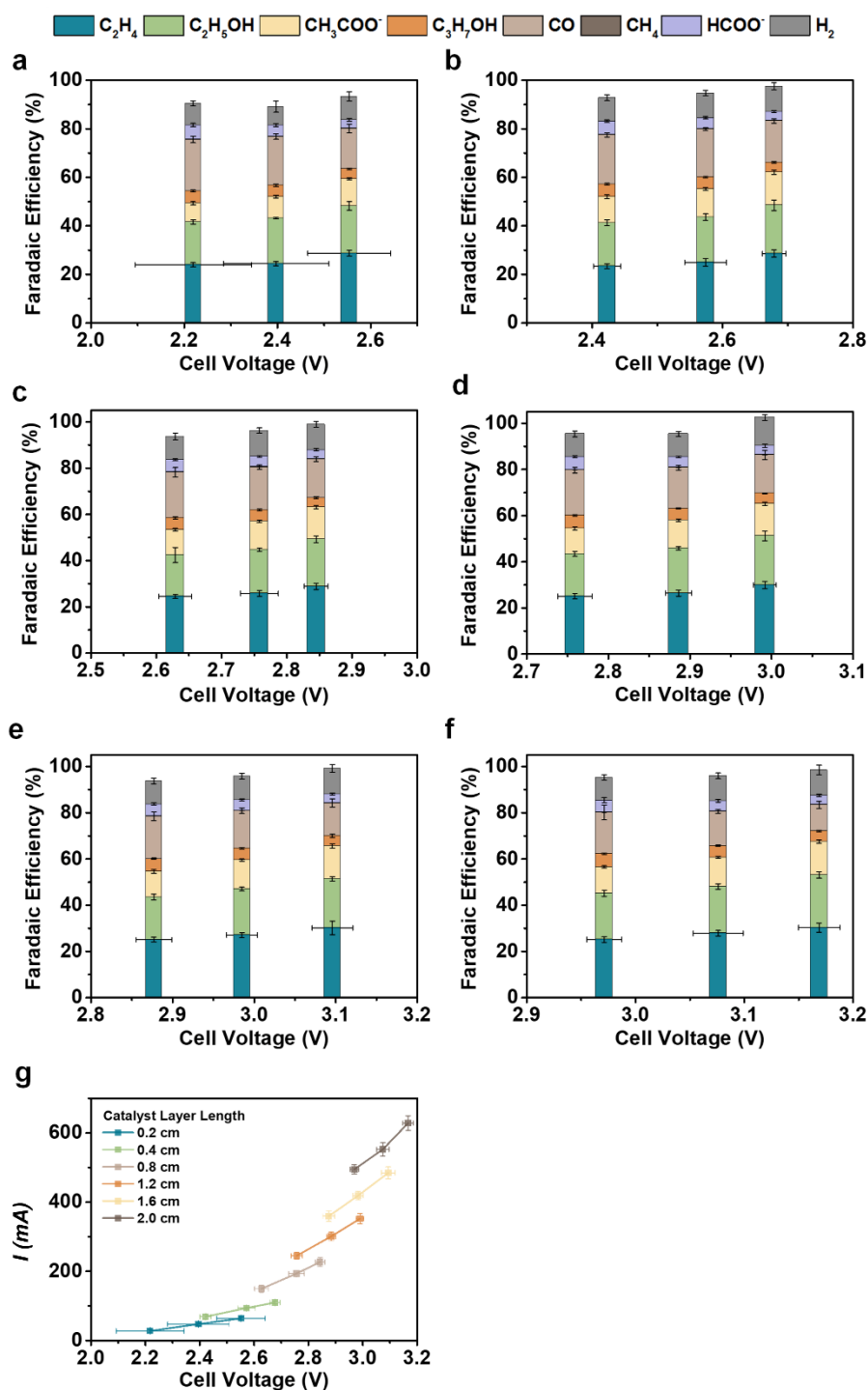
Supplementary Figure S5. (a) The electrochemically active surface-area measurements using the double-layer capacitance method. **(b)** Measured specific double-layer capacitance for the six Cu/Ag s-GDEs with various Cu CL lengths from 0.20 to 2.00 cm. The double-layer capacitance measurement was conducted in Ar-purged 1.0 M KOH in a H-type electrolyzer. To exclude the effect of carbon paper, the backside of the electrode was sealed with epoxy and only left the CL exposed. The scan rate varied from 10 to 100 mV s^{-1} in the non-Faradaic potential range. The obtained current was plotted as a function of the scan rate to derive the C_{dl} .



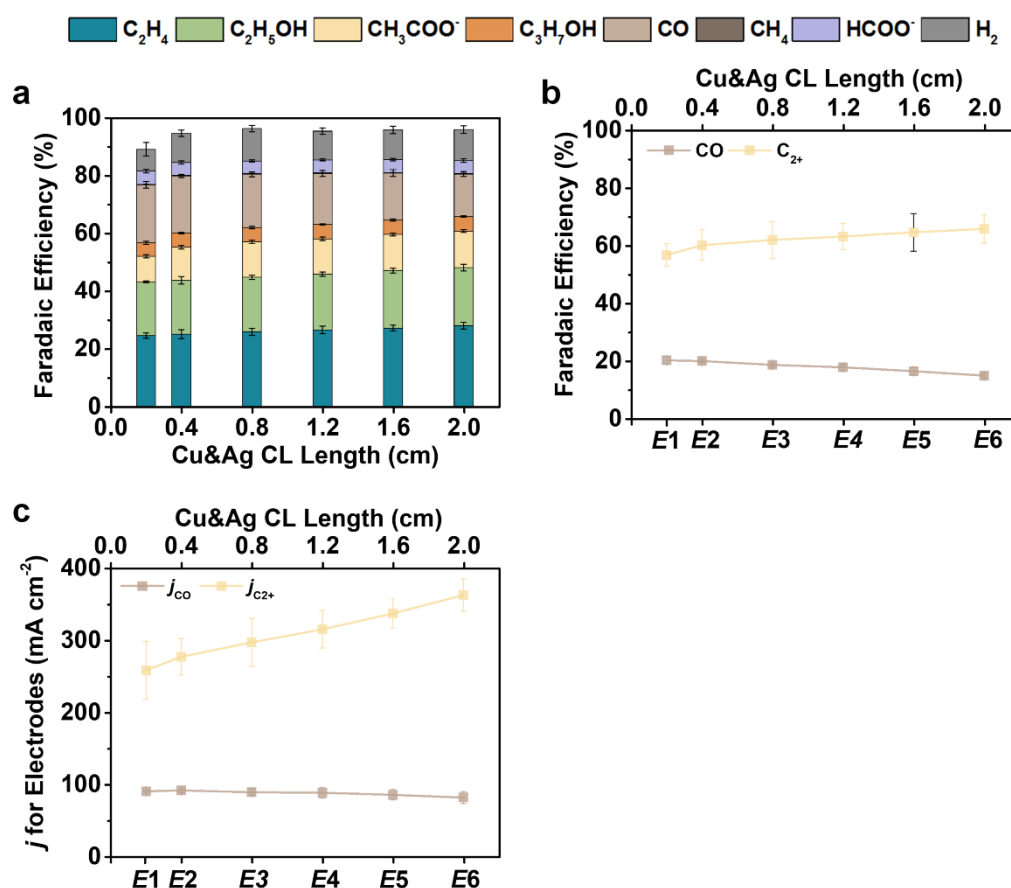
Supplementary Figure S6. (a) CO Faradaic efficiency and **(b)** partial current density (j_{CO}) for bare Ag and Cu gas-diffusion electrodes (GDEs) with comparable loading of 0.40 mg cm^{-2} . The error bars represent the standard deviation of measurements from three independent electrodes. From these results, it can be seen that for the Cu/Ag (1.00:0.05) s-GDE, which possesses a 0.04 mg Ag layer located in the inlet region of dimensions $0.50 \times 0.10 \text{ cm}^2$, the CO partial current (I_{CO}) generated by Ag is estimated to be -20.6 mA . The I_{CO} delivered by Cu should be around -5.4 mA since the I_{CO} is proportional to the area of Cu CL. Therefore, the CO from Ag accounts for 80% of the CO concentration at the inlet region for the Cu/Ag (1.00:0.05) s-GDE.



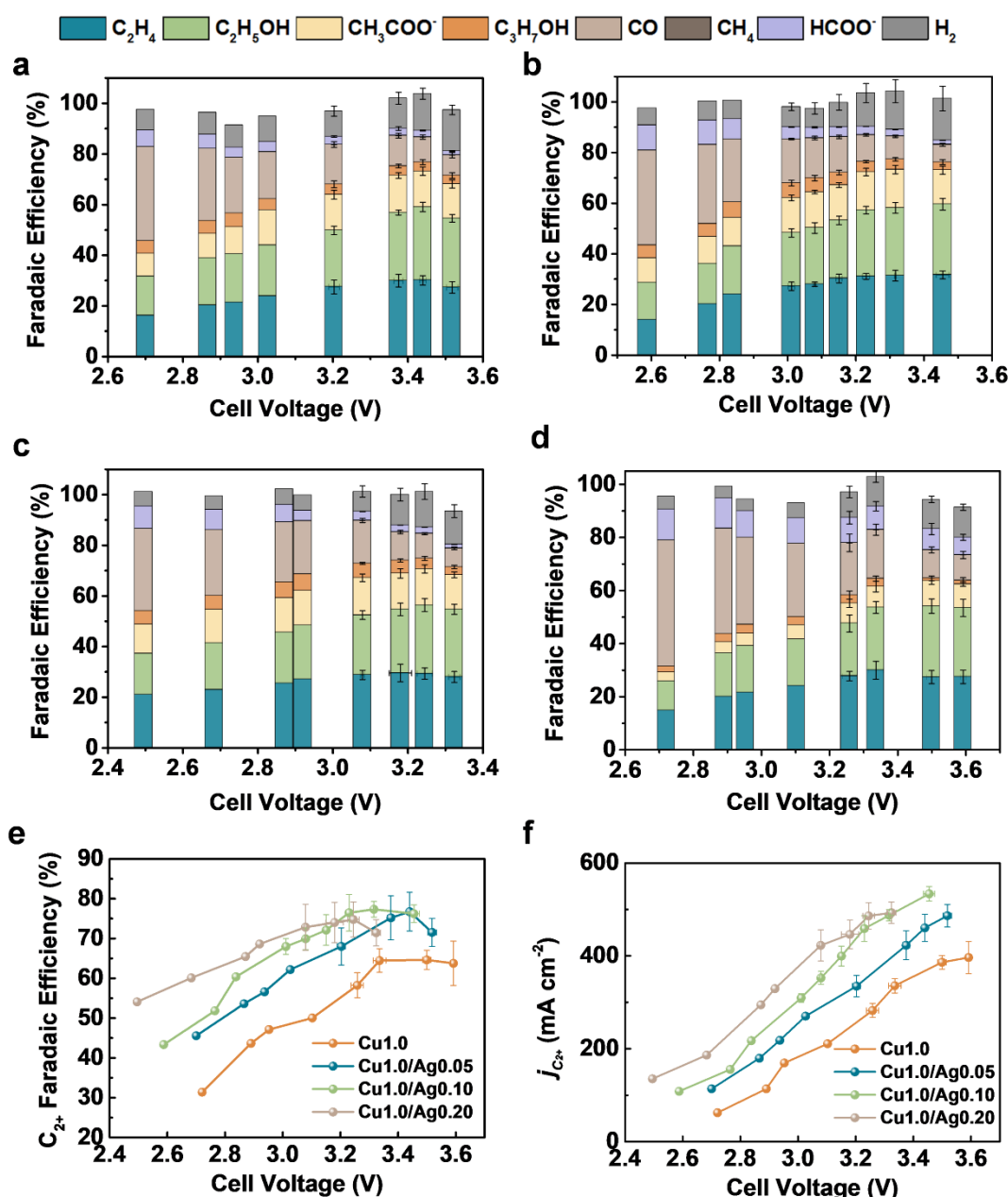
Supplementary Figure S7. The schematic of the preparation procedure for modified Cu/Ag 1-GDEs. Inset: the geometry of six 1-GDEs (from E₁ to E₆) with the dimensions of both Ag CL and Cu CL varying from W 0.50 × L 0.20 cm² to W 0.50 × L 0.20 cm².



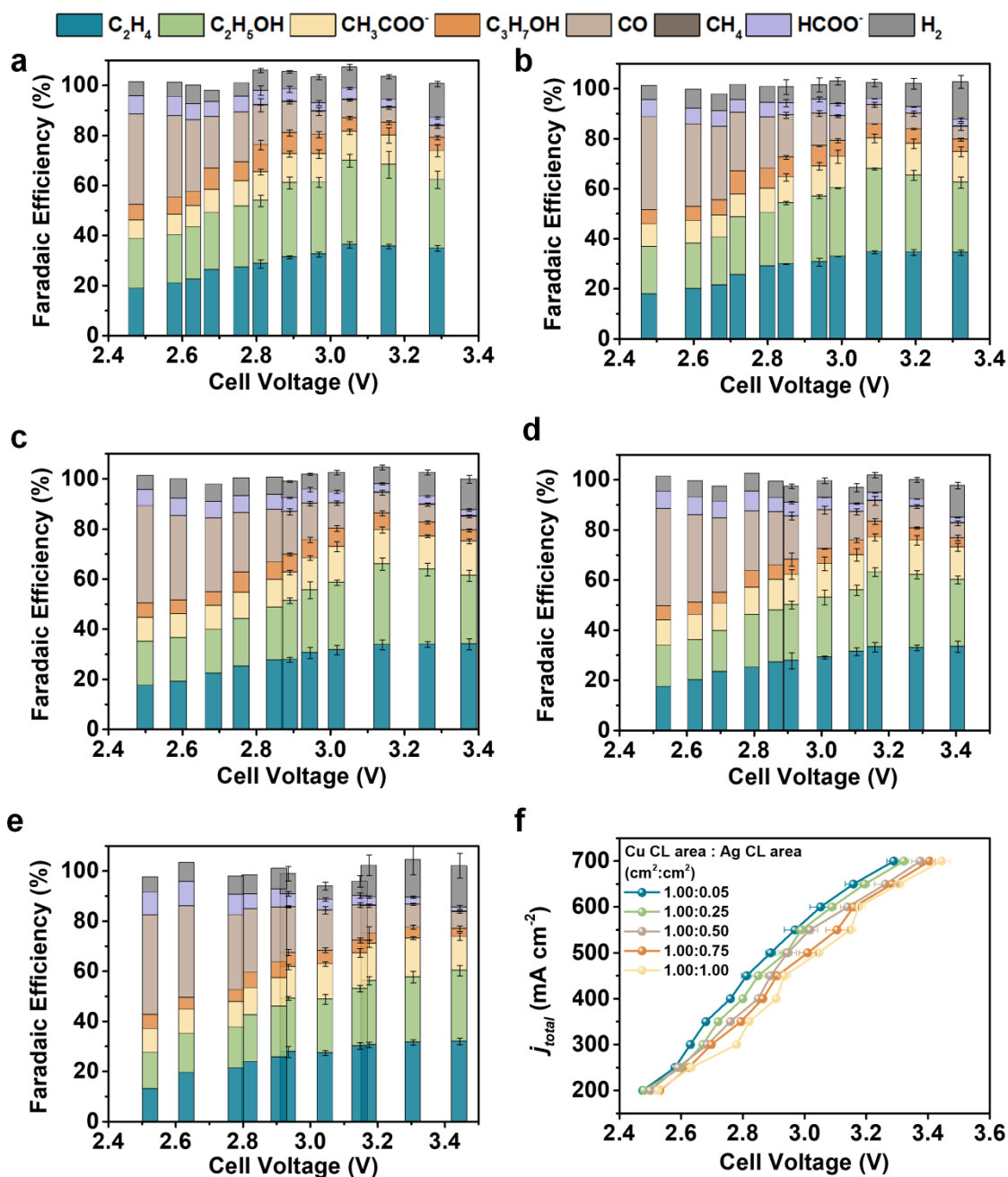
Supplementary Figure S8. Product distribution versus applied cell potential for the six Cu/Ag l-GDEs (from E_1 to E_6) with various Cu CL and Ag CL lengths of (a) 0.2 cm; (b) 0.4 cm; (c) 0.8 cm; (d) 1.2 cm; (e) 1.6 cm; (f) 2.0 cm. (g) The total current density for the corresponding six Cu/Ag l-GDEs. The cell voltage was IR corrected. The error bars represent the standard deviation of measurements from three independent electrodes.



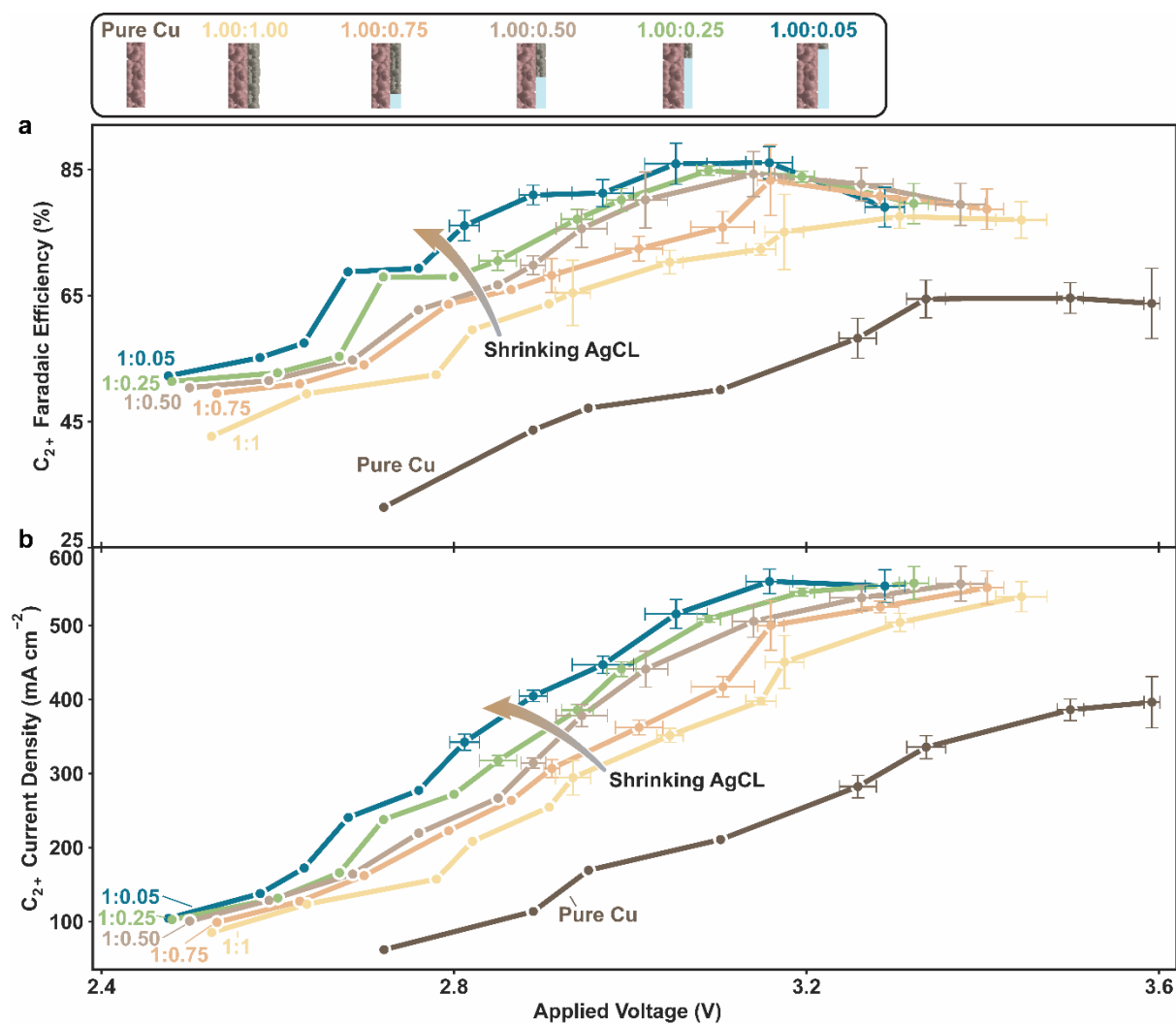
Supplementary Figure S9. (a) The product distribution under the cathode potential of -0.7 V versus RHE for the six Cu/Ag 1-GDEs (from E₁ to E₆) with both Cu CL and Ag CL lengths varying from 0.2 to 2.0 cm. (b-c) The corresponding (b) Faradaic efficiency and (c) partial current density of CO and C₂₊ products. The cathode potential was calculated by subtracting the measured anode potential from the IR-corrected applied cell voltage. The error bars represent the standard deviation of measurements from three independent electrodes.



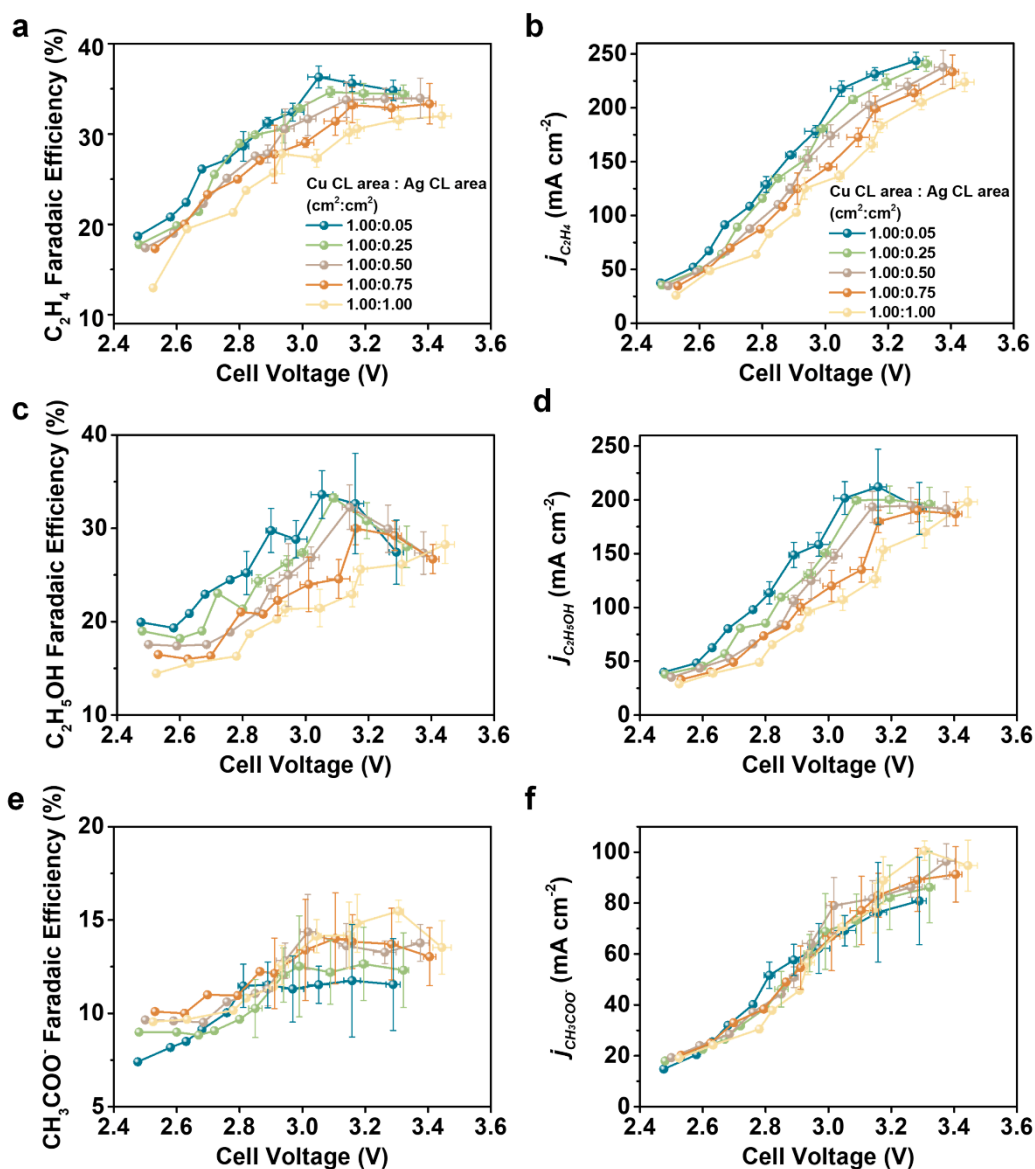
Supplementary Figure S10. Optimization of the Cu:Ag mass ratio before adjusting the area ratio. The product distribution versus the cell voltage for Cu/Ag l-GDEs with a Cu:Ag mass ratio of (a) 1.00:0.05, (b) 1.00:0.10, (c) 1.00:0.20, and (d) 1.00:0 (pure Cu GDE). (e-f) The (e) C₂+ faradaic efficiency and (f) j_{C_2+} for the corresponding electrodes. The Cu mass for all l-GDEs was kept at 0.40 mg and the electrode area was 1.0 cm², leading to a loading of 0.40 mg cm⁻². The performance was measured in an MEA electrolyzer. The error bars represent the standard deviation of measurements from three independent electrodes. The Cu/Ag l-GDEs with a Cu:Ag mass ratio of 1.00:0.10 show the best C₂+ product selectivity. Additionally, considering the thickness of Ag CL will build up as we shrink the Ag CL area, the lower mass is always preferred if the higher mass does not improve the performance much. Therefore, the obtained Cu (0.40 mg) and Ag (0.04 mg) mass were selected and applied to 1 cm² stacked s-GDEs.



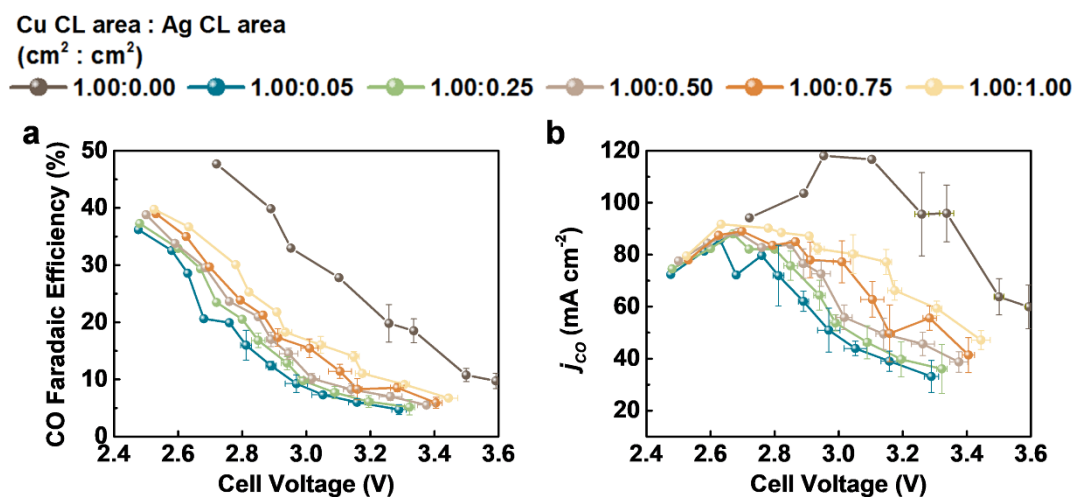
Supplementary Figure S11. The product distribution versus applied current density for Cu/Ag s-GDEs with different Cu CL: Ag CL area ratios of (a) 1.00:0.05; (b) 1.00:0.25; (c) 1.00:0.50; (d) 1.00:0.75; (e) 1.00:1.00. (f) Polarization curve for the above-mentioned five Cu/Ag s-GDEs. The error bars represent the standard deviation of measurements from three independent electrodes. The Cu CL area was kept at 1.0 cm^2 . The Cu mass was 0.40 mg corresponding to a Cu loading of 0.40 $mg\ cm^{-2}$. The Ag mass was kept at 0.04 mg but the loading varied with Ag CL area.



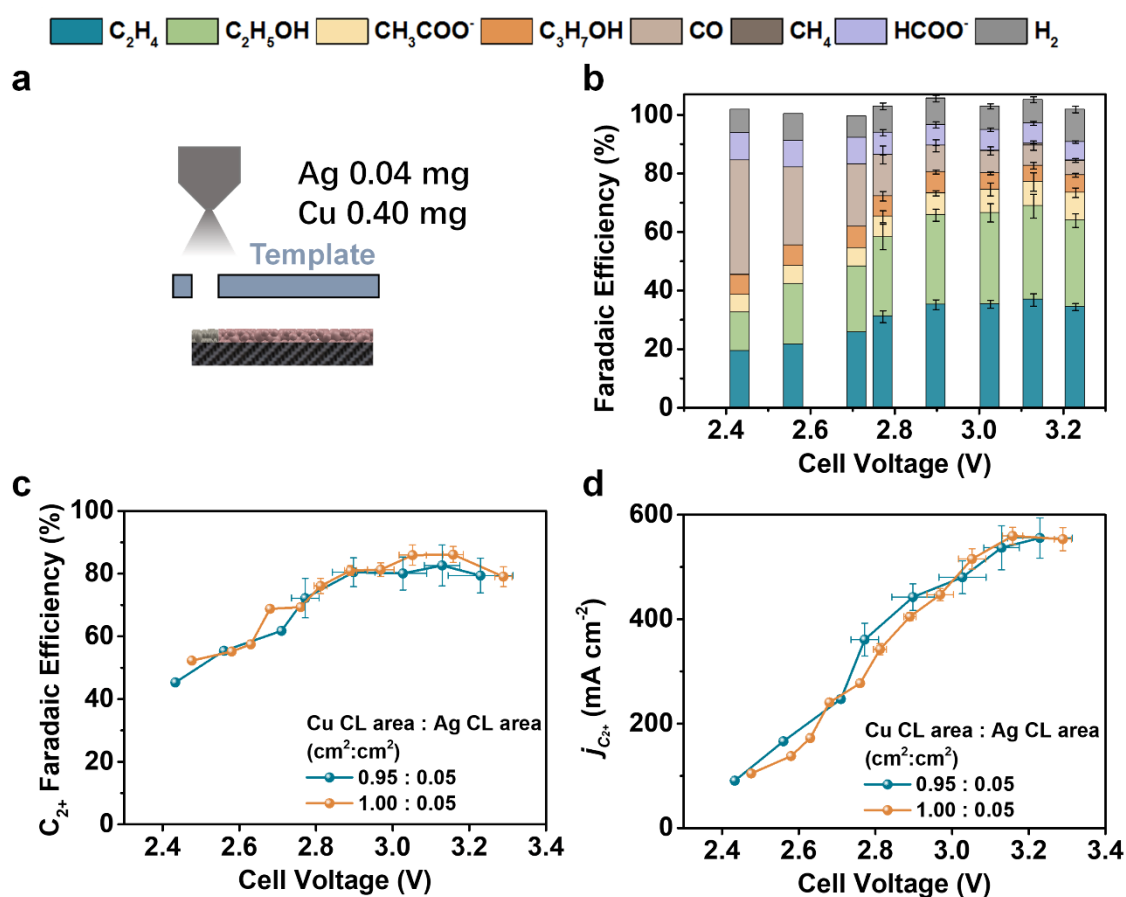
Supplementary Figure S12. The (a) C_{2+} FE and (b) C_{2+} current density for Cu/Ag s-GDEs with different Cu CL:Ag CL area ratios.

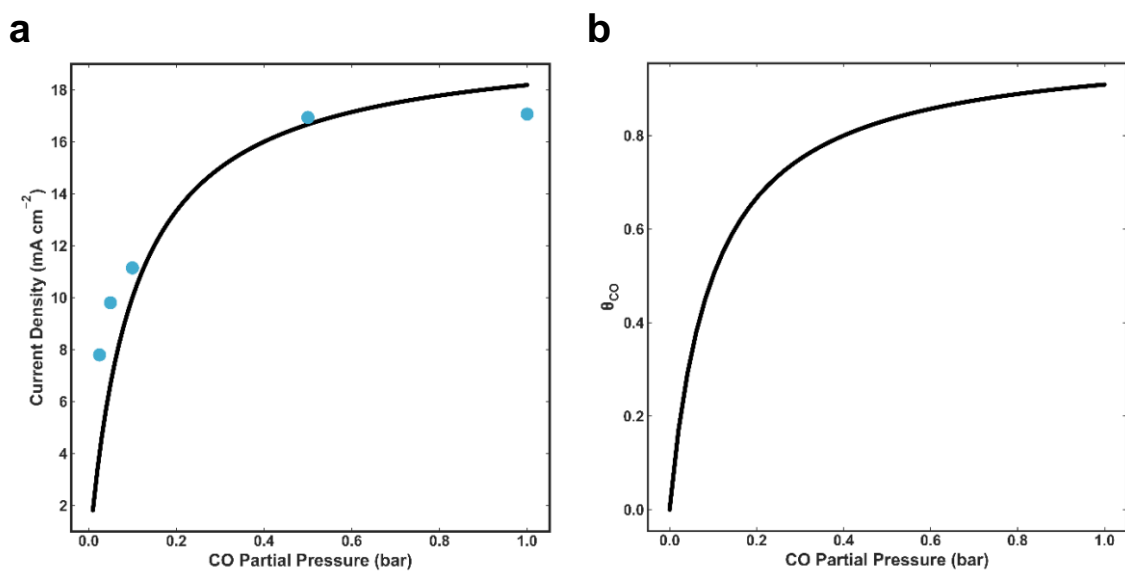


Supplementary Figure S13. (a) C_2H_4 Faradaic efficiency, (b) $j_{C_2H_4}$, (c) C_2H_5OH Faradaic efficiency, (d) $j_{C_2H_5OH}$, (e) CH_3COO^- Faradaic efficiency, and (f) $j_{CH_3COO^-}$ versus applied cell potential for five Cu/Ag s-GDEs with different Cu CL:Ag CL area ratios of 1.00:0.05, 1.00:0.25, 1.00:0.50, 1.00:0.75, and 1.00:1.00. The error bars represent the standard deviation of measurements from three independent electrodes.

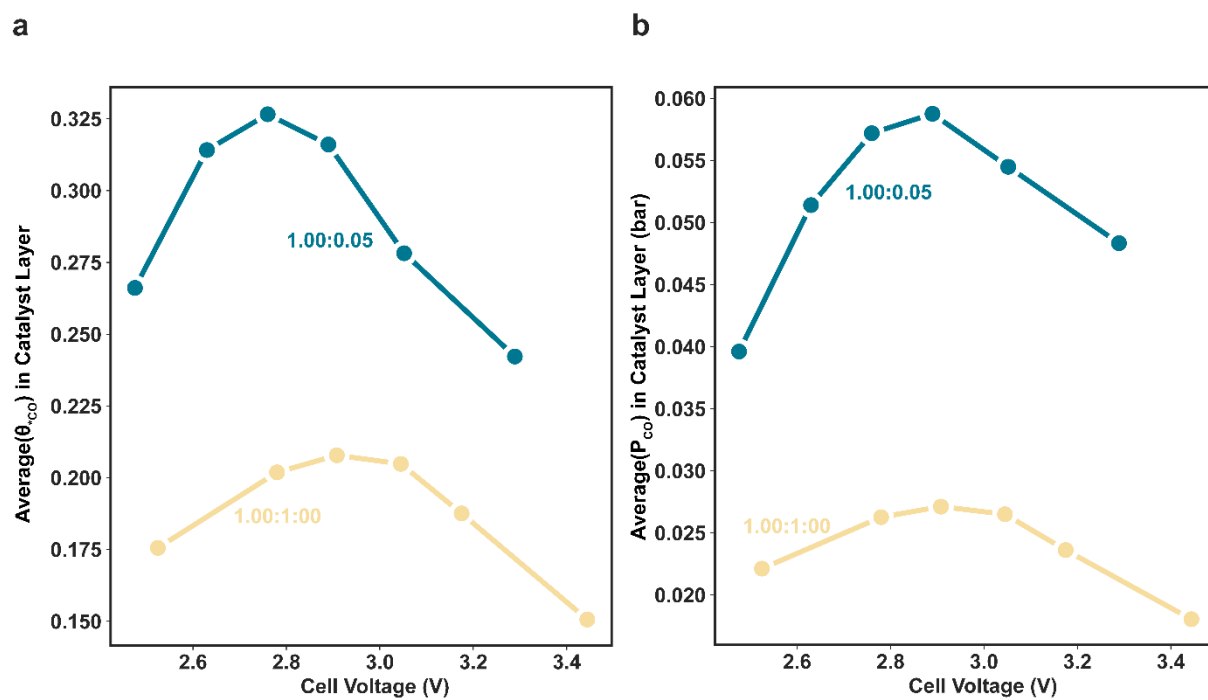


Supplementary Figure S14. (a) CO Faradaic efficiency and **(b)** CO partial current density versus applied cell voltage for the five Cu/Ag s-GDEs with different Cu:Ag area ratios of 1.00:0.05, 1.00:0.25, 1.00:0.50, 1.00:0.75, and 1.00:1.00 and the pure Cu GDE. The error bars represent the standard deviation of measurements from three independent electrodes.

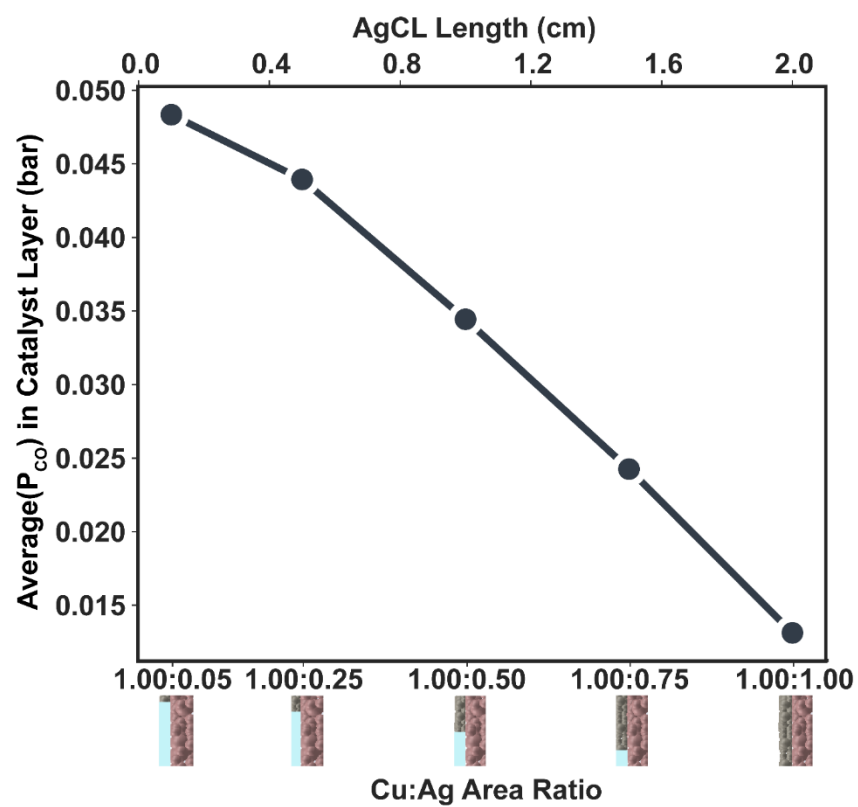




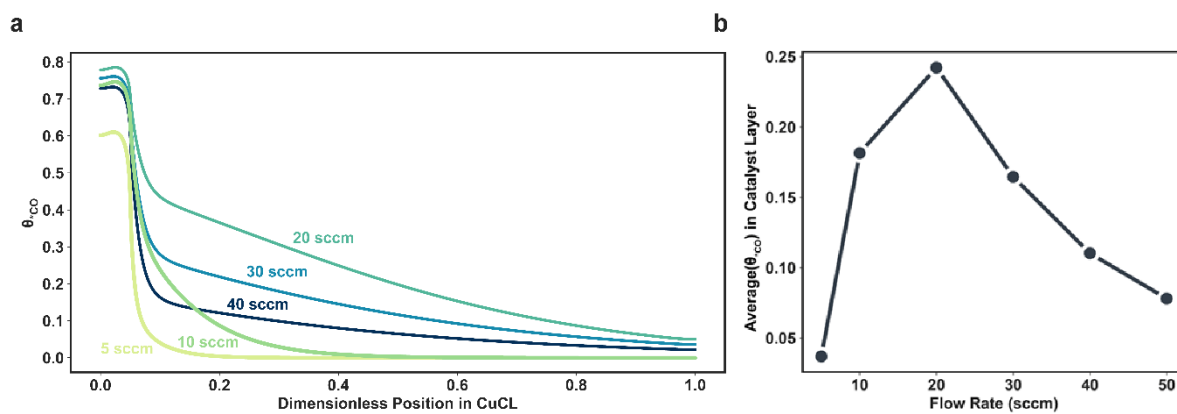
Supplementary Figure S16. (a) Fit of Langmuir adsorption model to experimental data by Li *et al.*³ **(b)** Modeled Langmuir adsorption, θ_{*CO} versus local CO partial pressure.



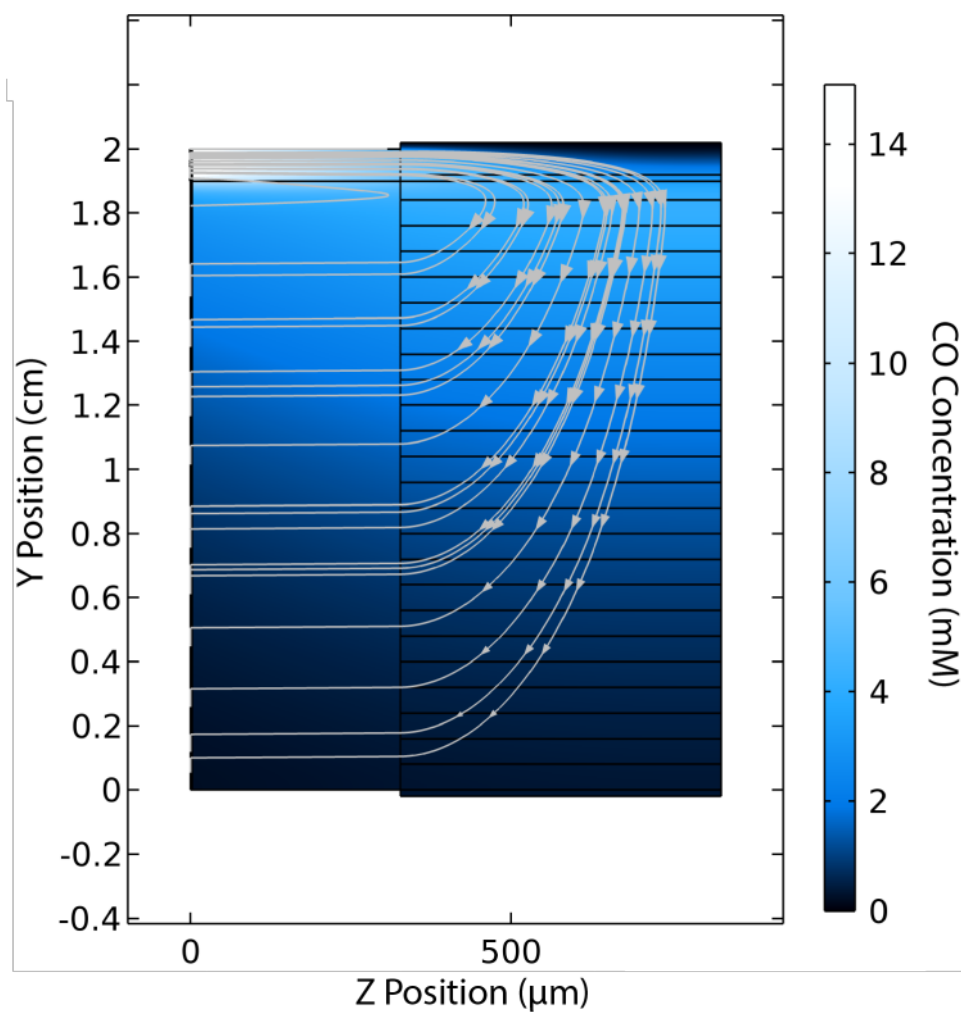
Supplementary Figure S17. Average (a) θ_{*CO} and (b) P_{CO} versus applied cell voltage for Cu/Ag s-GDEs with Cu Ag area ratios of 1.00 : 0.05, and 1.00 : 1.00.



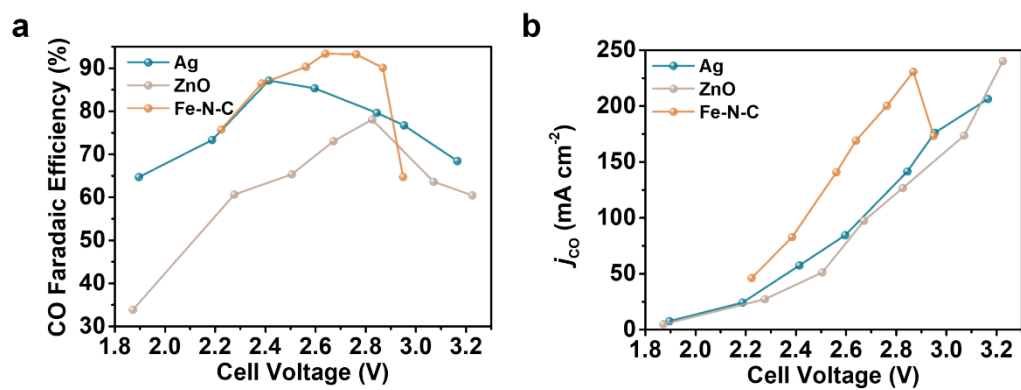
Supplementary Figure S18. Average P_{CO} versus Cu Ag area ratios of 1.00:0.05, 1.00:0.25, 1.00:0.50, 1.00:0.75, and 1.00:1.00.



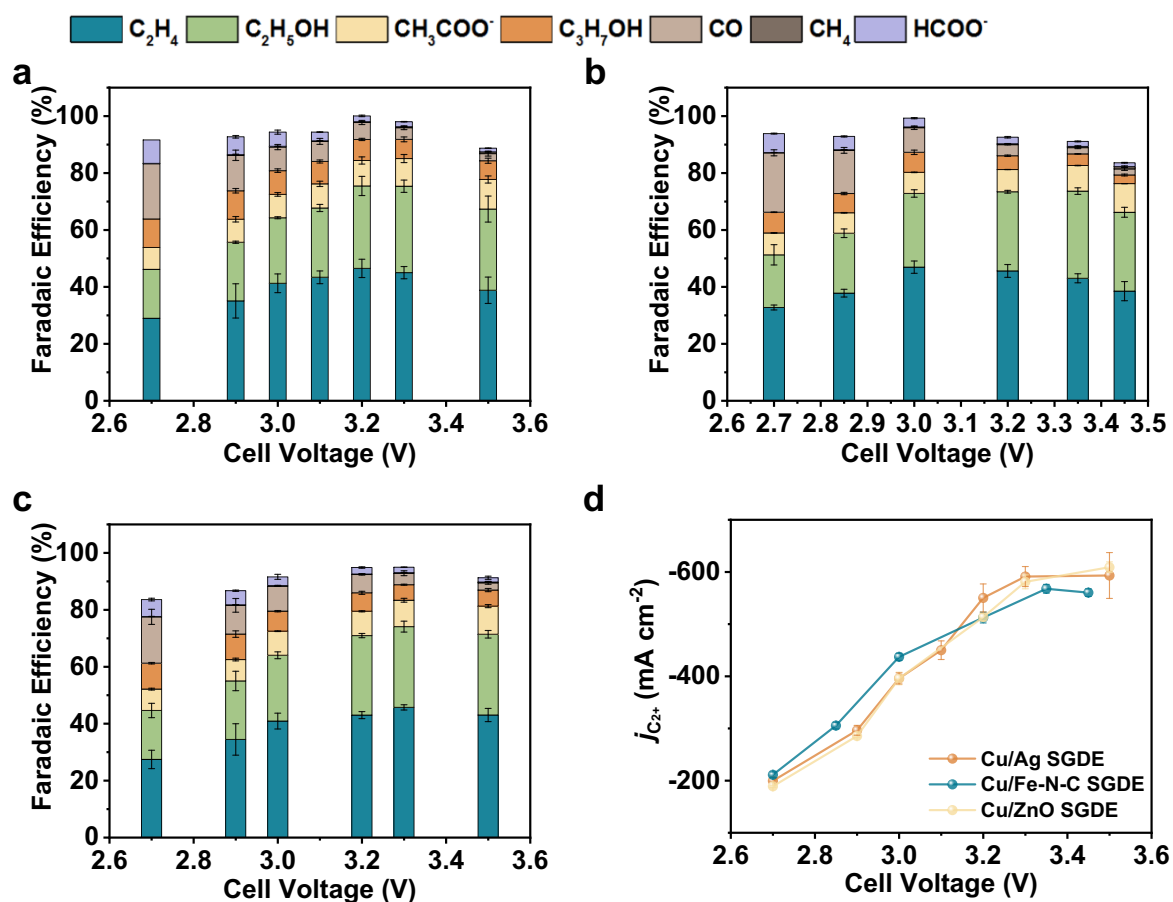
Supplementary Figure S19. (a) Simulated profile of θ_{*CO} within the CuCL for various CO₂ flow rates. **(b)** Average θ_{*CO} within the CuCL versus CO₂ flow rate.



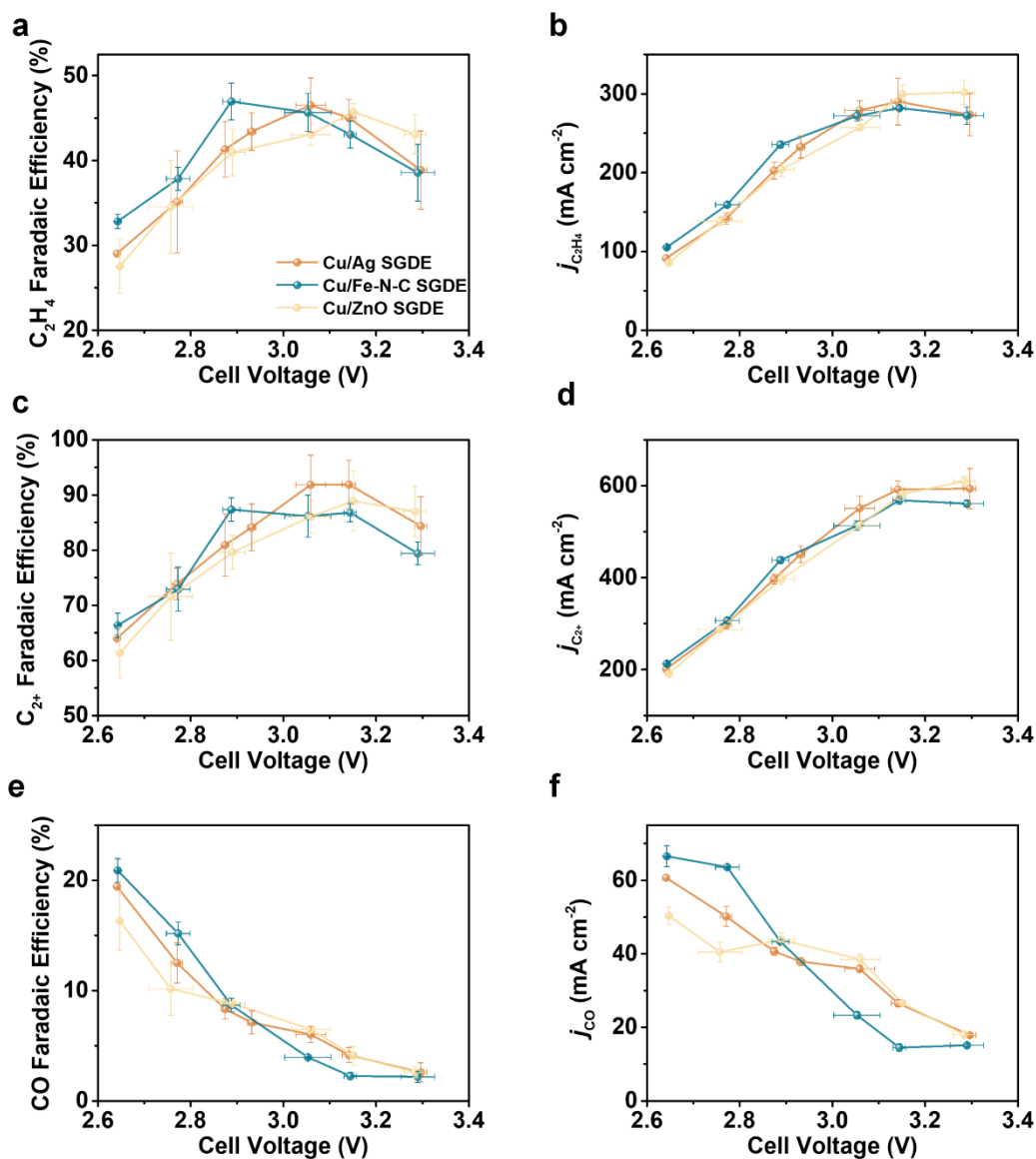
Supplementary Figure S20. Simulated CO flow profile within a Cu/Ag 1.00:0.05 s-GDE at an applied current density of 700 mA cm^{-2} .



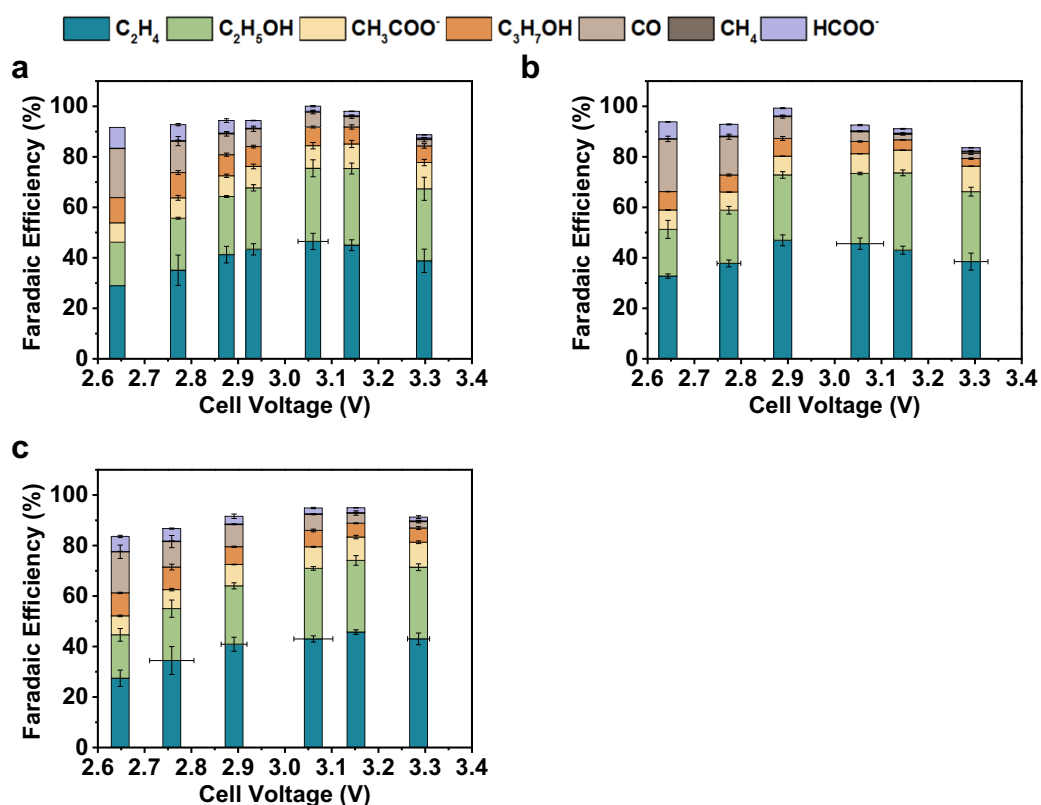
Supplementary Figure S21. (a) The CO faradaic efficiency and (b) j_{CO} versus applied cell voltage for three CO-selective catalysts such as Ag, ZnO, and Fe-N-C. The performance was measured in an MEA electrolyzer.



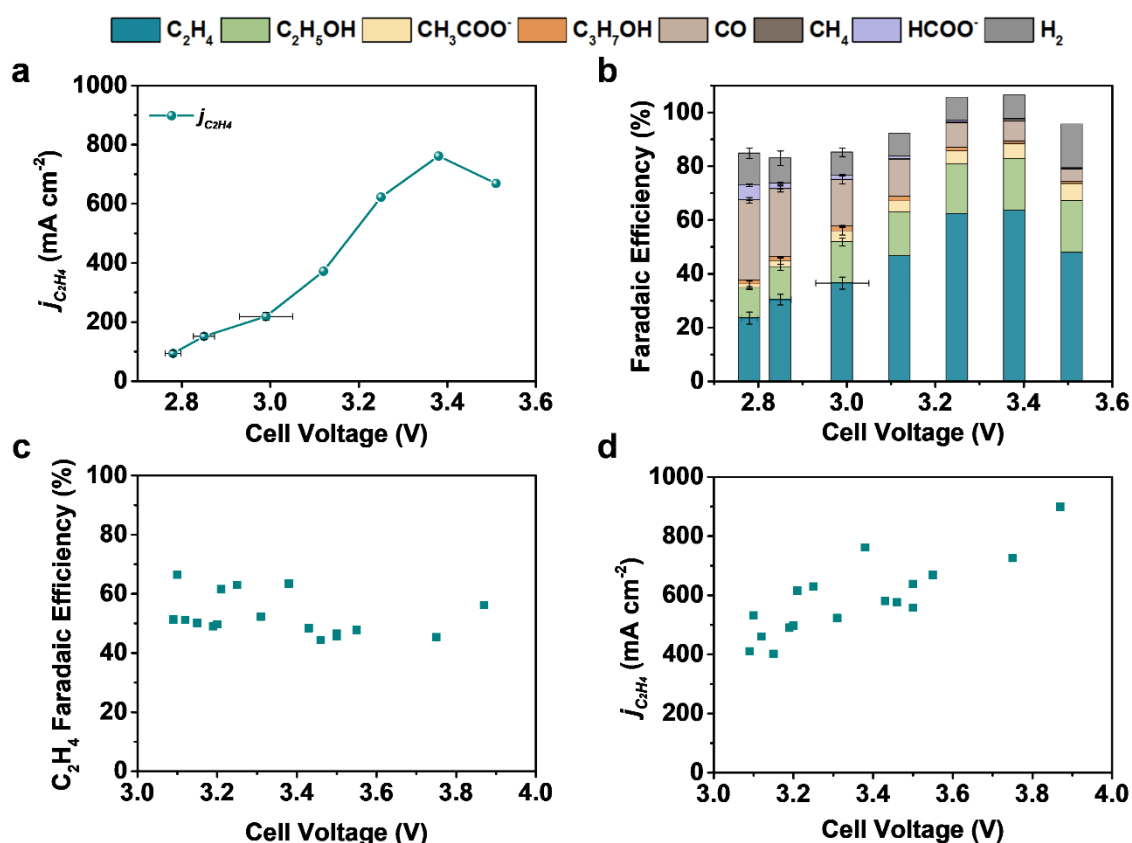
Supplementary Figure S22. The product distribution versus the applied cell voltage before IR-correction for (a) Cu/Ag s-GDE, (b) Cu/Fe-N-C s-GDE, and (c) Cu/ZnO s-GDE. (d) The j_{C2+} versus the applied cell voltage before IR-correction for the three electrodes mentioned above.



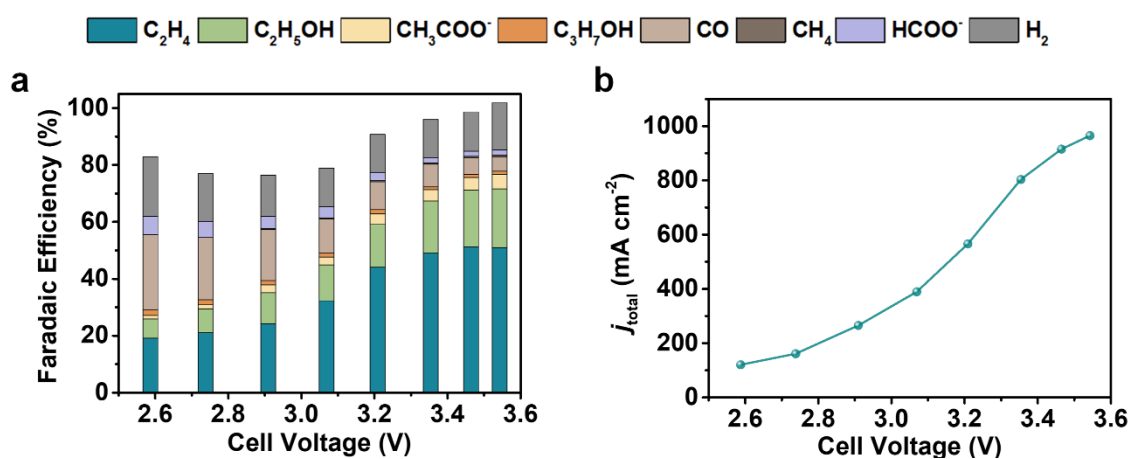
Supplementary Figure S23. The detailed CO₂ reduction performance for Cu/Ag s-GDE, Cu/Fe-N-C s-GDE, and Cu/ZnO s-GDE. **(a, c, and e)** faradaic efficiency and **(b, d, and f)** partial current density of **(a, b)** C₂H₄, **(c, d)** C₂⁺ products, and **(e, f)** CO for the three kinds mentioned above of s-GDE. The performance was measured in an MEA electrolyzer.



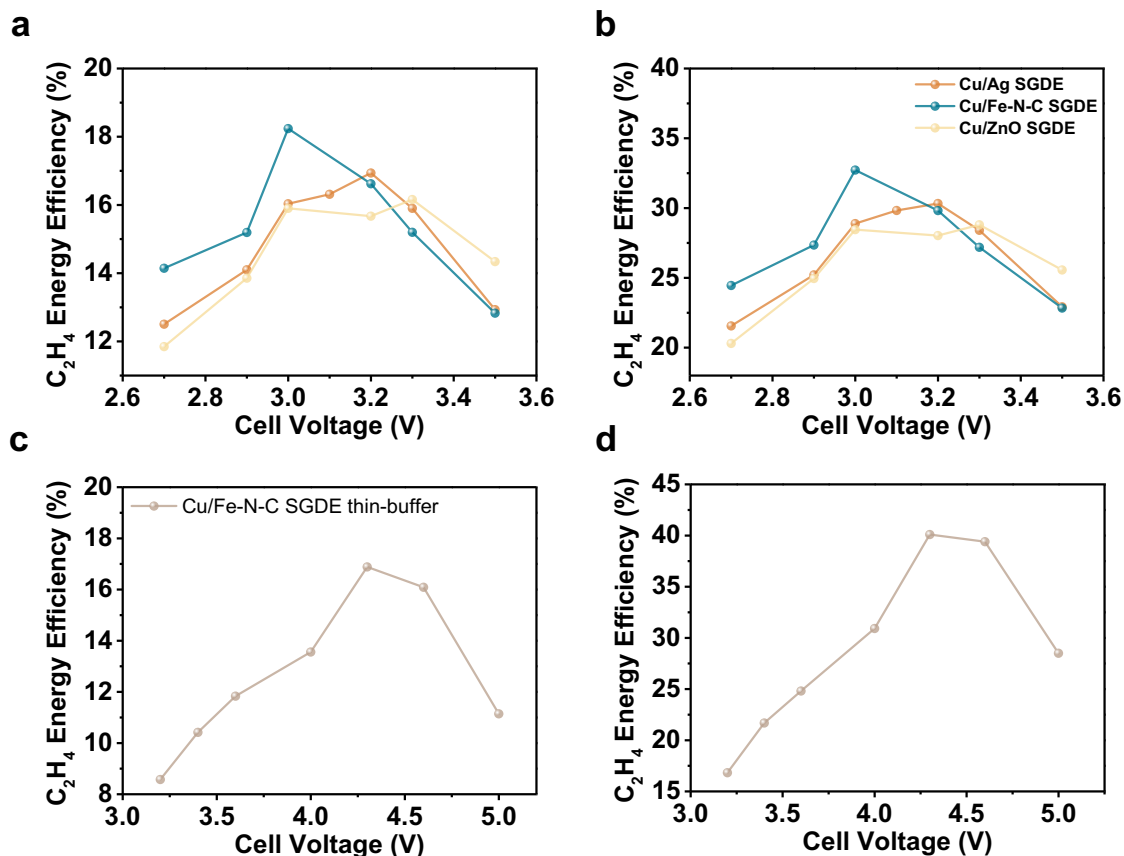
Supplementary Figure S24. The product distribution versus the applied cell potential for (a) Cu/Ag s-GDE, (b) Cu/Fe-N-C s-GDE, and (c) Cu/ZnO s-GDE. The performance was measured in an MEA electrolyzer. The error bars represent the standard deviation of measurements from three independent electrodes.



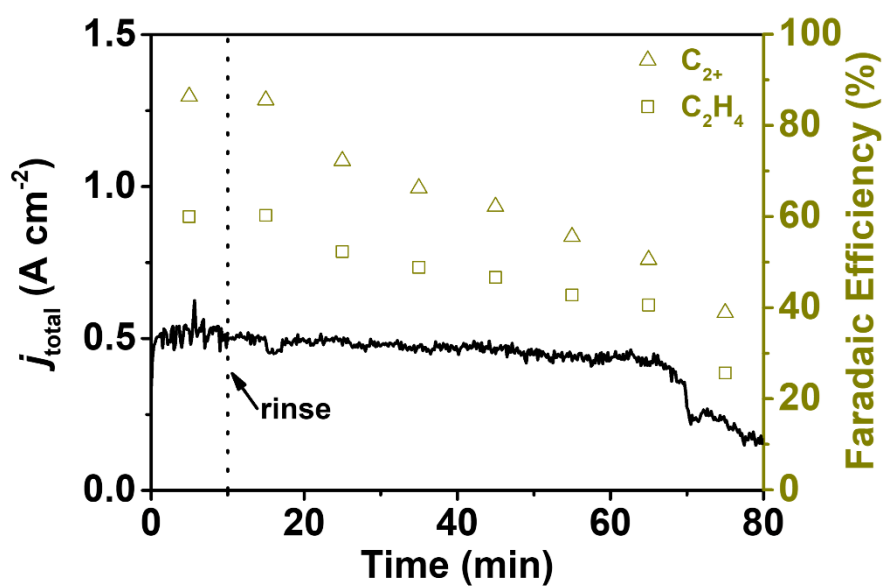
Supplementary Figure S25. (a) $j_{C_2H_4}$ versus applied cell potential and (b) product distribution for doubly-loaded Cu/Fe-N-C s-GDE tested in the thin-buffer flow cell. (c-d) The data points of (c) C_2H_4 Faradaic efficiency and (d) $j_{C_2H_4}$ at high cell potential regime from over 15 independent electrodes measurements. The error is significant under high current density due to uncontrollable flooding. Nonetheless, a Faradaic efficiency of over 60% for C_2H_4 is reproducible once the flooding is minimized.



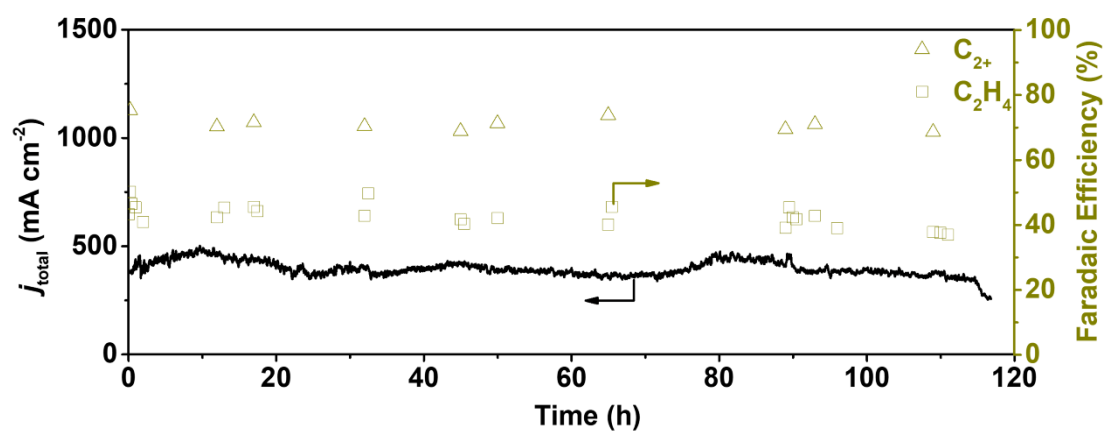
Supplementary Figure S26. (a) The Faradaic efficiency of CO₂R products and (b) j_{total} versus applied cell voltage for the pure Cu GDE (loading 0.80 mg cm⁻²) tested in a flow cell with a 2 mm cathodic buffer layer.



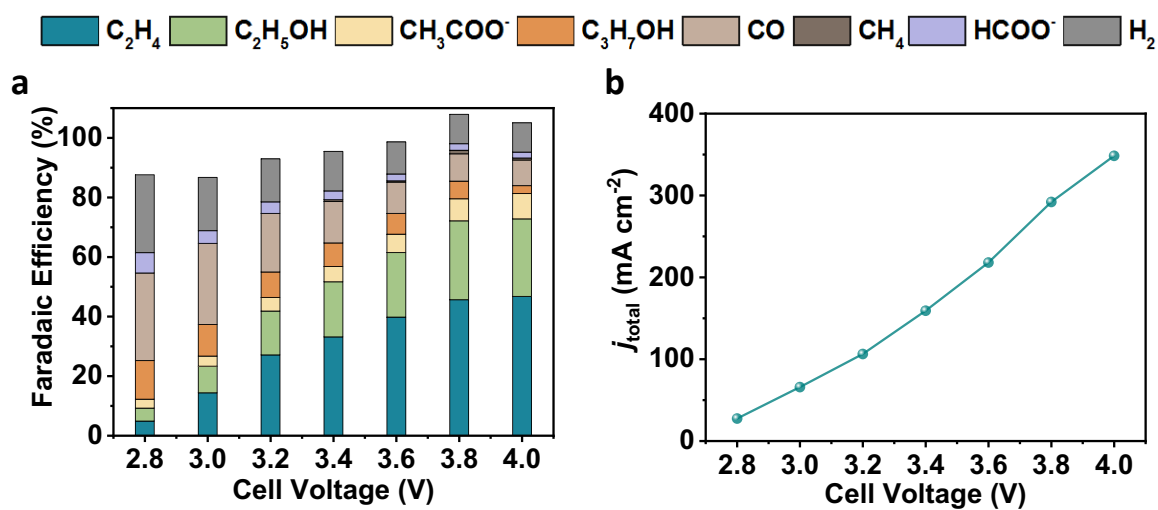
Supplementary Figure S27. (a) Full-cell energy efficiency and (b) half-cell energy efficiency of C_2H_4 production in an MEA electrolyzer for Cu/Fe-N-C s-GDE, Cu/Ag s-GDE, and Cu/ZnO s-GDE. (c) Full-cell energy efficiency and (d) half-cell energy efficiency of C_2H_4 production for Cu/Fe-N-C s-GDE in a flow cell including a 2 mm cathodic buffer layer.



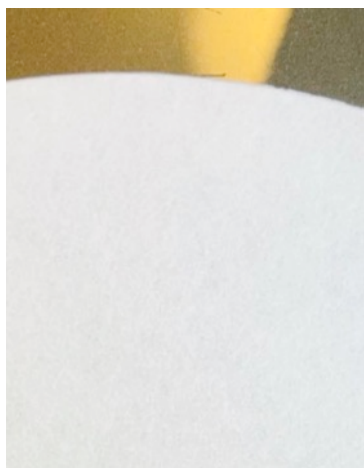
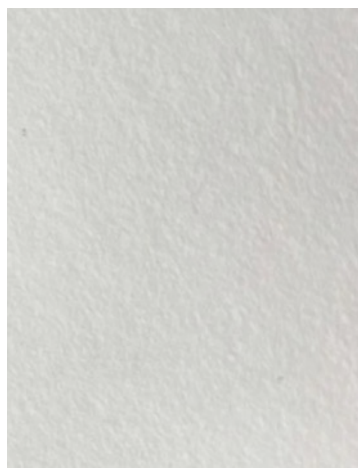
Supplementary Figure S28. Long-term stability test for the Cu/Fe-N-C s-GDE in the MEA electrolyzer. At 10th min, a dose of water was injected into the gas flow channel to remove the salt precipitates, followed by a 3 min blow-dry with Ar stream. After that, the test resumed.



Supplementary Figure S29. Long-term stability test for the Cu/Fe-N-C s-GDE in the thin-buffer (2 mm) flow cell.



Supplementary Figure S30. (a) Faradaic efficiency of all the products and (b) total current density versus the full cell voltage without IR correction for Cu/Fe-N-C s-GDE in the MEA cell and using 0.1 M $KHCO_3$ anolyte.

a**b**

Supplementary Figure S31. Photos of the Cu/Ag s-GDE **(a)** before and **(b)** after the epoxy sealing.

Supplementary Table S1. List of parameters used in the multiphysics simulation.

Parameter	Value	Units	Ref.
$L_{Channel}$	1	mm	
L_{GDL}	325	μm	1
L_{CuCL}	2	μm	
H_{cell}	2	cm	
W_{cell}	1	mm	
D_{CO,CO_2}	1.61×10^{-5}	$\text{m}^2 \text{s}^{-1}$	6
D_{CO_2,N_2}	1.64×10^{-5}	$\text{m}^2 \text{s}^{-1}$	6
D_{CO,N_2}	2.04×10^{-5}	$\text{m}^2 \text{s}^{-1}$	6
K_{CO}	10	atm^{-1}	8
MW_{CO}	28	g mol^{-1}	
MW_{CO_2}	44	g mol^{-1}	
MW_{N_2}	28	g mol^{-1}	
ϵ_m	0.75		2
$\kappa_{m,GDL}$	3.5×10^{-12}	m^2	2
$\kappa_{m,CuCL}$	1.0×10^{-15}	m^2	2

Supplementary Table S2. The CO generation rate, CO dimerization rate, and the ratio between CO dimerization rate and CO generation rate at different applied cell voltages for five Cu/Ag s-GDEs with Cu CL and Ag CL area ratio varying from 1.00:0.05 to 1.00:1.00 along with the control Cu GDE.

s-GDE	Cell Voltage (V)	CO generation rate (mA cm ⁻²)	CO consumption rate (mA cm ⁻²)	CO utilization towards C ₂ ⁺ formation (%)
Cu/Ag s- GDE (1.00 : 0.05)	3.28	-231.3	-198.1	85.7
	3.16	-236.3	-197.3	83.5
	3.05	-229.4	-185.5	80.9
	2.97	-208.7	-157.7	75.6
	2.89	-206.7	-144.7	70.0
Cu/Ag s- GDE (1.00 : 0.25)	3.32	-236.5	-200.4	84.8
	3.20	-235.4	-195.7	83.1
	3.09	-230.2	-184.0	79.9
	2.99	-210.6	-156.8	74.5
	2.94	-203.1	-138.7	68.3
Cu/Ag s- GDE (1.00 : 0.50)	3.37	-240.7	-202.0	83.9
	3.26	-239.5	-193.8	80.9
	3.14	-236.0	-186.4	79.0
	3.02	-216.2	-160.3	74.2
	2.95	-209.5	-136.9	65.3
Cu/Ag s- GDE (1.00 : 0.75)	3.40	-236.1	-194.7	82.5
	3.28	-245.6	-190.0	77.4
	3.16	-230.4	-180.7	78.4
	3.10	-214.8	-152.0	70.8
	3.01	-209.2	-132.0	63.1
Cu/Ag s- GDE (1.00 : 1.00)	3.44	-243.0	-195.8	80.6
	3.31	-244.3	-185.0	75.7
	3.18	-231.6	-165.3	71.4
	3.14	-222.9	-145.7	65.4
	3.05	-205.9	-125.7	61.0
Cu GDE	3.59	-201.3	-141.4	70.3
	3.50	-201.9	-138.2	68.4
	3.34	-214.6	-118.8	55.3
	3.26	-195.8	-100.3	51.2
	3.10	-190.6	-74.0	38.8

* The results of the CO generation and consumption rate were analyzed in Supplementary Note

Supplementary Table S3. The average CO residence time of the five different segmented Cu/Ag gas diffusion electrodes with Cu CL area: Ag CL area varies from 1.00: 0.05 to 1.00: 1.00.

Electrode	Average CO residence time (s)
Cu/Ag (1.00:0.05) s-GDE	0.146
Cu/Ag (1.00:0.25) s-GDE	0.131
Cu/Ag (1.00:0.50) s-GDE	0.113
Cu/Ag (1.00:0.75) s-GDE	0.094
Cu/Ag (1.00:1.00) s-GDE	0.075

Supplementary Table S4. Comparison of the CO₂ reduction performance in an MEA cell utilizing a low concentration bicarbonate anolyte.

Electrolyte	Cell voltage (V)	Current density (mA cm ⁻²)	C ₂ H ₄ Faradaic efficiency (%)	C ₂ + Faradaic efficiency (%)	Reference
0.1 M KHCO ₃	4	360	64	74	9
0.15 M KHCO ₃	3.7	65	60		10
0.1 M KHCO ₃	3.65	120	60		11
0.1 M KHCO ₃	4	150	42	64	12
0.1 M KHCO ₃	4	348	47	86	This work

Supplementary Note S1

The CO generation rate represents the partial current density of the surface adsorbed *CO, taking into account both the remaining CO product and the *CO hydrogenated into hydrocarbons and oxygenates. Therefore, the CO generation rate is the sum of j_{CO} and normalized partial current densities of hydrocarbons and oxygenates by the electron transfer number per CO reduced to a specific product as follows.

$$\text{CO generation rate} = j_{CO} + \frac{j_{CH_4}}{4} + \frac{j_{C_2H_4}}{3} + \frac{j_{C_2H_5OH}}{3} + \frac{j_{CH_3COO^-}}{2} + \frac{j_{C_3H_7OH}}{3} \quad (S14)$$

The CO dimerization rate is referred to the current density that generates the *CO that are consumed to form C_{2+} products as follows.

$$\text{CO dimerization rate} = \frac{j_{C_2H_4}}{3} + \frac{j_{C_2H_5OH}}{3} + \frac{j_{CH_3COO^-}}{2} + \frac{j_{C_3H_7OH}}{3} \quad (S15)$$

The ratio of CO dimerization rate over the CO generation rate directly illustrates the utilization efficiency of CO that goes toward C_{2+} products.

Supplementary Note S2

As shown in **Supplementary Figure S6**, Ag possesses substantially higher intrinsic activity for the generation at CO. However, due to the loading ratio employed in the study (10 Cu: 1 Ag by mass), Cu is an appreciable source of CO provided for C-C coupling in our tandem catalysts, however, not all of that is further reduced due to the location in which it is generated. For instance, at 3.16 V, where the Cu-Ag tandem electrode achieves its optimum C₂₊ production performance, Ag and Cu generate j_{CO} of around -206.0 and -108.0 mA cm⁻², respectively. Since the amount of Ag is 0.04 mg, the CO generation from Ag is approximately 20.6 mA cm⁻², yet it is concentrated at the inlet.

Supplementary Note S3

Calculation of residence time for s-GDEs with varying Cu/Ag area ratio. The CO residence time can be roughly estimated by calculating the average residence time (τ_{ave}) of supplementary CO for each specific s-GDE structure as shown in equation S16. The calculation is made under the assumption that the quantity of Ag is the constant on these five s-GDEs, and the Ag CL thickness is uniform on each s-GDE.

$$\tau_{ave} = \frac{\sum_{i=1}^n (\frac{V}{Q} \times x_i)}{n} \quad (S16)$$

where the V is the total volume of the flow channel; Q is the gas flow rate; n is the number of CO molecules. Here we assume that these different s-GDE structures generate the same amount of supplementary CO because they possess identical quantities of Ag; x_i is a linear factor between 0 and 1 representing the position of the CO molecular i in the flow channel. The inlet is 1, and the outlet is 0.

Following this formulation, for the case that the flow channel volume is 0.5 mL and the gas flow rate is 20 sccm, the average CO residence time for each mentioned s-GDE structure is listed in **Supplementary Table S3**.

References

- 1 Schweiss, R., Meiser, C., Damjanovic, T., Galbiati, I. & Haak, N. SIGRACET gas diffusion layers for PEM fuel cells, electrolyzers and batteries. *White paper SGL Group* (2016).
- 2 Kas, R. *et al.* Along the Channel Gradients Impact on the Spatioactivity of Gas Diffusion Electrodes at High Conversions during CO₂ Electroreduction. *ACS Sustainable Chemistry & Engineering* **9**, 1286-1296 (2021).
- 3 Li, Y. C. *et al.* Binding Site Diversity Promotes CO₂ Electroreduction to Ethanol. *Journal of the American Chemical Society* **141**, 8584-8591, doi:10.1021/jacs.9b02945 (2019).
- 4 Bui, J. C., Kim, C., Weber, A. Z. & Bell, A. T. Dynamic Boundary Layer Simulation of Pulsed CO₂ Electrolysis on a Copper Catalyst. *ACS Energy Letters*, 1181-1188, doi:10.1021/acsenerylett.1c00364 (2021).
- 5 Wang, L. *et al.* Electrochemical Carbon Monoxide Reduction on Polycrystalline Copper: Effects of Potential, Pressure, and pH on Selectivity toward Multicarbon and Oxygenated Products. *ACS Catalysis* **8**, 7445-7454, doi:10.1021/acscatal.8b01200 (2018).
- 6 Weng, L.-C., Bell, A. T. & Weber, A. Z. A systematic analysis of Cu-based membrane-electrode assemblies for CO₂ reduction through multiphysics simulation. *Energy & Environmental Science*, doi:10.1039/d0ee01604g (2020).
- 7 Nitopi, S. *et al.* Progress and Perspectives of Electrochemical CO₂ Reduction on Copper in Aqueous Electrolyte. *Chem Rev* **119**, 7610-7672, doi:10.1021/acs.chemrev.8b00705 (2019).
- 8 Li, J. *et al.* Constraining CO coverage on copper promotes high-efficiency ethylene electroproduction. *Nature Catalysis*, doi:10.1038/s41929-019-0380-x (2019).
- 9 Ozden, A. *et al.* High-Rate and Efficient Ethylene Electrosynthesis Using a Catalyst/Promoter/Transport Layer. *ACS Energy Letters* **5**, 2811-2818, doi:10.1021/acsenerylett.0c01266 (2020).
- 10 Wang, Y. *et al.* Catalyst synthesis under CO₂ electroreduction favours faceting and promotes renewable fuels electrosynthesis. *Nature Catalysis* **3**, 98-106, doi:10.1038/s41929-019-0397-1 (2019).
- 11 Li, F. *et al.* Molecular tuning of CO₂-to-ethylene conversion. *Nature* **577**, 509-513, doi:10.1038/s41586-019-1782-2 (2020).
- 12 Gabardo, C. M. *et al.* Continuous Carbon Dioxide Electroreduction to Concentrated Multi-carbon Products Using a Membrane Electrode Assembly. *Joule* **3**, 2777-2791, doi:10.1016/j.joule.2019.07.021 (2019).